

Elsevier Editorial System(tm) for Journal of
Natural Gas Science & Engineering
Manuscript Draft

Manuscript Number: JNGSE-D-18-01722R2

Title: Numerical modeling of CO₂ fracturing by the phase field approach

Article Type: Full Length Article

Keywords: CO₂ fracturing; CO₂ fluid flow; phase field

Corresponding Author: Professor Yongxing Shen, Ph.D.

Corresponding Author's Institution: Shanghai Jiao Tong University

First Author: Mostafa Mollaali, Ph.D.

Order of Authors: Mostafa Mollaali, Ph.D.; Vahid Ziae Rad, Ph.D.;
Yongxing Shen, Ph.D.

Abstract: We propose a phase field model to simulate CO₂ fracturing under an isothermal condition. We take advantage of the ability of the phase field approach in predicting fracture initiation and branching, and also to avoid tracking the fracture path. We model the CO₂ as a compressible fluid by modifying Darcy's law. In particular, we assume the permeability is correlated to the phase field value by an exponential function. The dependence of the CO₂ density as a function of the pressure is captured by the Span-Wagner equation of state. The computed breakdown pressure values show good agreement with analytical solutions and experimental results.

Research Data Related to this Submission

There are no linked research data sets for this submission. The following reason is given:

Data will be made available on request

Response to reviewer comments on ‘Numerical modeling of CO₂ fracturing by the phase field approach’

Mostafa Mollaali^a, Vahid Ziae-Rad^b, Yongxing Shen^{a,*}

^a*University of Michigan – Shanghai Jiao Tong University Joint Institute, Shanghai Jiao Tong University, Shanghai, 200240, China*

^b*Department of Civil Engineering, Isfahan University of Technology, Isfahan 84156-83111, Iran*

We thank the reviewers again for their constructive comments. Below we respond to each of the comments, along with the corresponding changes of the manuscript. All changes to the previous submission are marked **in blue** in the revised version.

Comments from Reviewer #2

To the best of my knowledge, the proposed method is novel and the paper is well written. All my questions have been answered in this revision. From my opinion, this paper is acceptable for publication without further revision.

Comments from Reviewer #3

The modification does not solve my major concerns.

1. Regarding Question 4: Mandel’s problem is a typical poroelastic problem. It is not for incompressible fluid. The principles behind the poroelastic borehole are the same as those in the Mandel’s problem. The authors did not demonstrated typical poroelastic response through borehole pressurization.

We did try to solve Mandel’s problem with our algorithm, and the results are satisfactory. Nevertheless, we do not plan to include it in the manuscript, because in some sense it repeats the numerical example in Section 4.2, as both couple porous flow and the displacement of the porous medium.

In the sequel, we first describe how we solved Mandel’s problem with our algorithm. Consider a 2D rectangular domain of width $2a$ and height $2b$ occupied by a saturated poroelastic material. Constant compression forces are applied on

*Corresponding author
Email address: yongxing.shen@sjtu.edu.cn (Yongxing Shen)

rigid impermeable plates $y = \pm b$ with a magnitude of $2F$, see the configuration in Figure 1. The load is applied instantaneously at $t = 0^+$. At the right edge ($x = \pm a$) the sample can be drained while the lateral boundaries are free of stress.

We only model a quarter of the sample due to symmetry. The sample is assumed to be under plane strain conditions. The following boundary conditions are imposed:

$$\begin{aligned} p &= 0 && \text{on } x = a, \\ u_2 &= U_2(b, t) && \text{on } y = b, \\ u_1 &= 0 && \text{on } x = 0, \\ u_2 &= 0 && \text{on } y = 0. \end{aligned}$$

where $U_2(b, t)$ is the value of Mandel's closed form solution at $y = b$ [Y. Abousleiman, A.-D. Cheng, L. Cui, E. Detournay, J.-C. Roegiers, Mandel's problem revisited, *Geotechnique* 46 (2) (1996) 187–195]. The remaining boundary conditions are traction free boundary conditions.

Based on the analytical solution, as the compression load $2F$ is imposed, an instantaneous pressure increase and the following deformation responses are expected:

$$\begin{aligned} p(x, y, 0^+) &= \frac{FB(1 + \nu_u)}{3a}, \\ u_1(a, y, 0^+) &= \frac{F\nu_u}{2G}, \\ u_2(x, b, 0^+) &= -\frac{Fb(1 - \nu_u)}{2Ga}. \end{aligned}$$

The material parameters for rock and fluid are given in Table 1. Using our proposed algorithm in combination with the fixed-stress split method (see [43][44], which we have now also cited in the manuscript, see Section 3), we solved the numerical problem for $t_f = 6s$ in 600 equal time steps. Figure 2 shows our numerical results and the analytical solution for pore pressure. Excellent agreement is observed. Figure 3 shows the pore pressure developed in the sample during consolidation.

A comment on Mandel's problem follows here. It is true that this problem is a typical poroelastic problem. However, it would somehow repeat our second verification example (see Section 4.2) where the porous flow is coupled with the porous medium's displacement. The example in Section 4.2 solved by Detourney and Cheng [56] has been used in a few works, e.g., [11][57], to verify the solution to the poroelastic response of a pressurized borehole. For these reasons, we preferred not to include Mandel's problem in the manuscript.

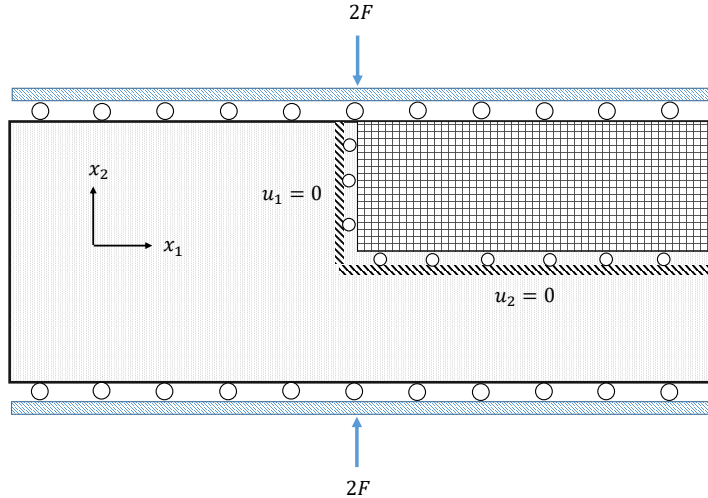


Figure 1: Schematic view of Mandel's problem. An instantaneous compression force $2F$ is applied on the horizontal edges. Due to symmetry, only a quarter of the sample is modeled with proper boundary conditions.

Table 1: Mandel's problem: Input parameters according to [43].

Parameters	symbol	unit	value
Young's modulus	E	MPa	1
Poisson's ratio	ν	—	0.2
Biot coefficient	α	—	1.
Permeability	k_0	m^2	1
Viscosity	μ	MPa·s	1
Length	a	m	2.5
Height	b	m	1
Load	F	MN	2.5
Skempton coefficient	B	—	1
Drained Poisson's ratio	ν_u	—	0.5
Biot's modulus	M	MPa	∞

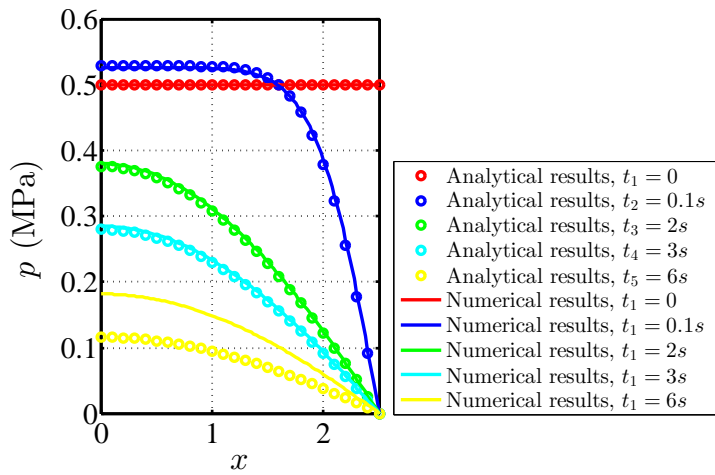
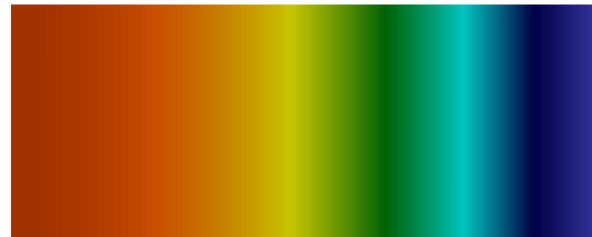


Figure 2: Mandel's problem: change of pore pressure in time. Excellent agreement is observed with the analytical solution.



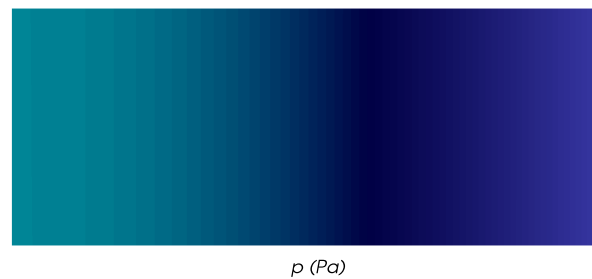
(a)



(b)



(c)



(d)

Figure 3: Pressure profile at different stages (3a) $t = 0.1s$, (3b) $t = 2s$, (3c) $t = 3s$, and (3d) $t = 6s$. At very early stages, the pressure rises rapidly in response to the instantaneous loading, then gradually decays to zero.

The phase field method for hydraulic fracture modeling is indeed successfully verified through semi-analytical solutions in other researchers' work. However, this does not indicate all the models utilizing the phase field method can be correctly verified through the semi-analytical solutions. The authors have to demonstrate that the model in this paper can match the semi-analytical solutions. I cannot understand why the authors think it is not necessary to verify their model just because the verification of the same method is already performed by other researchers.

Let us reiterate that our model for CO₂ treats it as a *compressible* fluid. None of existing papers that models fracturing with compressible CO₂ verifies with asymptotic semi-analytical solutions with hydraulic fracturing, the latter of which are based on an *incompressible* assumption of the fluid. Compressible fluids behave very differently from incompressible ones.

For verifying our model, we have not only checked the convergence of the discretization parameters for space and time, but also compared our examples in the manuscript against various solutions: the Hubbert-Willis (H-W) solution [60], the Haimson-Fairhurst (H-F) solution [61], the Sneddon and Lowengrub solution [58], and the Detourney and Cheng solution [56].

In response to the reviewer's request, we have reached out by applying our compressible formulation to the equation of state of water [R. T. Fernandez. Natural Convection from Cylinders Buried in Porous Media. PhD thesis, University of California; 1972] for a fracturing problem in the toughness-dominated regime (K-vertex), in order to compare our solution with the KGD model [J. Geertsma and F. De Klerk, A rapid method of predicting width and extent of hydraulically induced fractures, Journal of Petroleum Technology 21 (12) (1969) 1–571]. The parameters are given in Table 2. Figure 4 plots the evolution of the maximum fracture aperture of our numerical results and the KGD analytical solution. A good agreement is observed. Nevertheless, the fracture length evolution and the injection pressure do not agree well (not shown). This might be due to the over-extrapolation of the formulation to a fracturing fluid (water) that the formulation was not intended to model.

2. Regarding Question 2: All the given three references assume that grains are incompressible, which could be used approximately for soil. But this study is not about soil, it is about reservoir rock. There would not be too many people in the petroleum industry using this assumption in simulations.

It is true that including more complex assumptions for grains can lead to a more realistic model. However, we can cite a few works in which the grains for the reservoir are assumed incompressible: [M. Sheng, G. Li, S. N. Shah, X. Jin, Extended finite element modeling of multi-scale flow in fractured shale gas reservoirs, in: SPE Annual Technical Conference and Exhibition, Society of Petroleum Engineers, 2012, pp. SPE-159919-MS] and [A. Verruijt, Theory and Problems of Poroelasticity, 2013]. Thus, we believe the assumption adopted here is not too much out of the norm.

Table 2: Parameters for the comparison of KGD solution using the equation of state of water (a compressible formulation).

Parameters	symbol	unit	value
Young's modulus	E	MPa	6×10^3
Poisson's ratio	ν	—	0.34
Critical energy release rate	g_c	MPa·mm	0.306
Biot coefficient	α	—	0.85
Porosity	ϕ	—	0.01
Initial permeability	k_0	mm ²	1×10^{-12}
Dynamic viscosity of water	μ	MPa·s	7.9×10^{-3}
Initial pressure	p_0	MPa	0.1
Final time	t_f	s	500
Flow rate	$v \cdot n$	mm ² /s	5

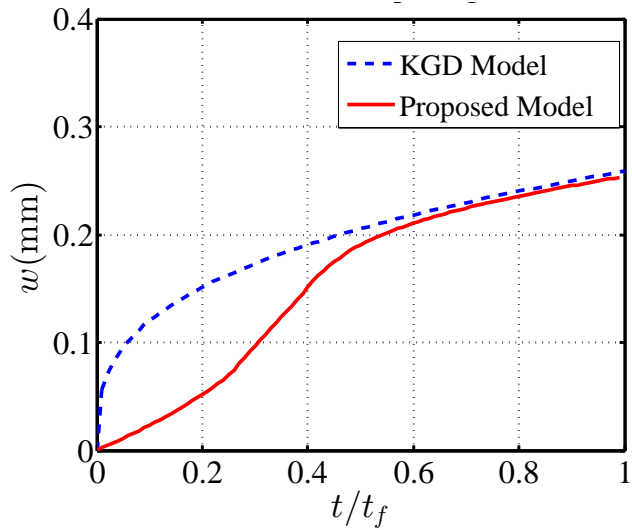


Figure 4: Verification of maximum fracture width for a toughness-dominated regime with KGD analytical solution [Geertsma and de Klerk, 1969].

3. Regarding Question 3: The discretization of the weak form is for solid part of a poroelastic model. The fluid flow part is entirely ignored.

In Appendix A.2 of the first revision, the discretization for fluid part was already provided. Moreover, we added one extra reference at the beginning of Appendix A for the implementation details.

In summary, the sequential coupling through volume strain is not correct; the model is not verified correctly, the correctness of the numerical model presented here is unknown.

We hope our response has clarified most of the issues.

*Highlights (for review)

- We propose a phase field model to simulate CO₂ fracturing, where we solve a coupled system consisting of: (i) mass balance with modified Darcy's equation, and (ii) a dissipative potential energy with the phase field.
- CO₂ is treated as a compressible fluid under an isothermal condition in a porous medium by using the Span-Wagner equation of state.
- The implementation is verified through three examples. The predicted breakdown pressure agrees well with analytical solutions and, within 30%, with experiments.

1
2
3
4
5
6
7
8
9
10
11
12
13
14
15
16
17
18
19
20
21
22
23
24
25
26
27
28
29
30
31
32
33
34
35
36
37
38
39
40
41
42
43
44
45
46
47
48
49
50
51
52
53
54
55
56
57
58
59
60
61
62
63
64
65

Numerical modeling of CO₂ fracturing by the phase field approach

Mostafa Mollaali^a, Vahid Ziae-Rad^b, Yongxing Shen^{a,*}

^a*University of Michigan – Shanghai Jiao Tong University Joint Institute, Shanghai Jiao Tong University, Shanghai, 200240, China*

^b*Department of Civil Engineering, Isfahan University of Technology, Isfahan 84156-83111, Iran*

Abstract

We propose a phase field model to simulate CO₂ fracturing under an isothermal condition. We take advantage of the ability of the phase field approach in predicting fracture initiation and branching, and also to avoid tracking the fracture path. We model the CO₂ as a compressible fluid by modifying Darcy's law. In particular, we assume the permeability is correlated to the phase field value by an exponential function. The dependence of the CO₂ density as a function of the pressure is captured by the Span-Wagner equation of state. The computed breakdown pressure values show good agreement with analytical solutions and experimental results.

Keywords: CO₂ fracturing, CO₂ fluid flow, phase field

2010 MSC: 65K10

1. Introduction

Shale gas is the natural gas trapped within the shale, or mudstone reservoir. Shale is a fine-grained, sedimentary rock composed of clay minerals and silt-sized particles. The shale has low permeability so that it significantly inhibits the gas flow from the reservoir rocks to the production wells. As a result, the economic feasibility of shale gas development relies on the effective stimulation of the reservoirs [1]. Shale gas has become an energy source of increasing worldwide interest due to the two technologies that have become mature in industry: horizontal drilling and hydraulic fracturing technique [2].

To date, water-based fluids are the most important fluids regularly used in the commercial shale gas due to their ready availability and low cost. But there are also some disadvantages to use water-based fluids, namely water shortage, contamination of underground water, and low fracturing performance. Also, hydraulic fracturing cannot avoid the clay swelling problem in shale [2]. Due

*Corresponding author

Email address: yongxing.shen@sjtu.edu.cn (Yongxing Shen)

1
2
3
4
5
6
7
8
9 15 to these problems, researchers actively investigate non-aqueous (see [3]) and
10 non-fluid fracturing techniques such as explosive based method [4].

11 Carbon dioxide (CO_2) is one of the non-aqueous fracturing fluids that is
12 considered to be used for fracturing. CO_2 as a fracturing fluid has been success-
13 fully applied to fracturing unconventional gas reservoirs decades ago [5]. Since
14 the critical temperature of CO_2 is 31.1°C , once the pressure exceeds its critical
15 pressure of 7.38 MPa, it will change to the supercritical state [6]. It can be
16 injected down-hole either in liquid or supercritical state. The main benefits of
17 CO_2 as a fracturing fluid include reducing consumption of water and water con-
18 tamination, keeping clays (smectite and illite) stabilized, and preventing metal
19 leaching and chemical interactions.
20

21 Brown [7] proposed CO_2 as a fracturing fluid and circulating fluid in geother-
22 mal energy extraction. Middleton *et al.* [8] investigated the potential of using
23 CO_2 as a fracturing fluid for commercial scale of shale production. In the lab-
24 oratory scale, Ishida *et al.* [9, 10] conducted fracturing experiments by using
25 supercritical CO_2 . Also, some researchers investigated the effect of different
26 fracturing fluids [11, 12].

27 There exist two general approaches for modeling fracture. One is discrete
28 models for fracture where the geometrical discontinuity is modeled by modi-
29 fying the geometry of intact structure [13, 14, 15, 16]. The other is smeared
30 crack models where the discontinuity is distributed over a finite width, such as
31 the phase field [17] and the gradient-enhanced damage methods [18]. In this
32 approach, an additional unknown and a length scale are introduced.
33

34 Phase field modeling of fracture has gained popularity since the beginning of
35 this century. The phase field model by Bourdin *et al.* [17] is essentially a regular-
36 ization of the variational formulation of brittle fracture by Francfort and Marigo
37 [19]. What makes the phase field an attractive approach can be attributed to
38 its convenience in simulating complex fracture processes, including crack ini-
39 tiation, propagation, branching and merging. Compared to discrete fracture
40 descriptions, the phase field approaches avoid tracking the complicated crack
41 geometry; instead, the crack evolution is a natural outcome of the numerical
42 solution to a constrained optimization problem. Thus, it significantly decreases
43 the implementation difficulty, especially when dealing with 3D problems.
44

45 Bourdin *et al.* [20] have adopted the phase field approach to model hydraulic
46 fracturing in impermeable media by considering the force that fluid pressure
47 exerts on fracture surfaces. Afterwards, phase field approaches for hydraulic
48 fracture in porous media based on Biot's equations and the theory of porous
49 media have been investigated by many researchers.
50

51 Mikelić *et al.* [21] model pressurized fracture in porous media by combining
52 the Biot theory and phase field approach. To minimize code modifications for
53 adopting the phase field approach with an existing reservoir simulator, Yoshioka
54 and Bourdin [22] have proposed an efficient framework by modifying the Darcy
55 law. Wick *et al.* [23] have developed a model to simulate fluid-filled fracture
56 propagation coupled to a reservoir simulator. Also, they have used a single
57 pressure equation for the entire fractured domain by introducing a function to
58 distinguish between reservoir and fracture domains. Mauthe and Miehe [24] have
59
60
61
62
63
64
65

coupled the phase field hydraulic fracture and porous media fluid flow by using a permeability decomposition. Ehlers and Luo [25] have combined the theory of porous media (TPM) and the phase field approach to fracture. Also, Culp *et al.* [26] have applied the phase field approach to fracture in CO₂ sequestration.
In most cases researchers have supposed the fracturing fluid is incompressible or slightly compressible. Recently, Heider and Markert [27] proposed a method to model the pore fluid which is considered compressible.

The objective of the paper at hand is to propose a phase field model to investigate the effect of CO₂ as a compressible fracturing fluid under the isothermal condition, as the first step towards such modeling. For this purpose, we have adopted the phase field approach to model fracturing in porous media according to Mikelić *et al.* [21]. We model the CO₂ flow as a compressible fluid by modifying Darcy's law. We suppose permeability is correlated to the phase field value by an exponential function. The CO₂ density varies significantly with pressure, which is captured by the Span-Wagner equation of state [28].

In the remaining paper we will proceed as follows: a description of the fracture problem is given in Section 2, including the governing equations of the solid and the fluid flow. Afterwards, the numerical discretization and algorithm are constructed in Section 3. Then Section 4 provides numerical examples and discussions, where we will show that our results for the breakdown pressure agree well with not only widely used analytical solutions but also, within a reasonable error, with experimental results. Finally Section 5 draws conclusions.

2. Mathematical model

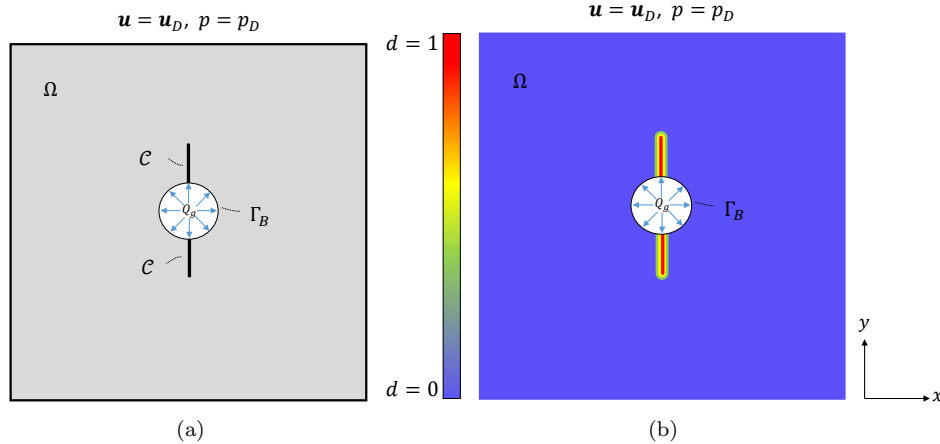
This section describes the mathematical model we will adopt for CO₂ fracturing. For convenience we will confine ourselves to the two-dimensional plane strain case, but the formulation is applicable to three dimensions with minimal changes. During the CO₂ fracturing process, the gas penetrates into the rock around the borehole and the injecting pressure causes the fracture to propagate. Thus, fracture propagation is a coupled phenomenon involving the gas flow inside the fracture and in the entire porous medium, the rock deformation, and the fracture propagation in the rock mass. In the following, in Section 2.1 we introduce the phase field method for fracture and derive the governing equations for the deformation and fracture propagation in the porous medium. Then, in Section 2.2 we present the governing equations for the gas flow within the porous medium. It is worth mentioning that compressible CO₂ exhibits a transport behavior different from that of slightly compressible fluids such as water and oil, due to its large compressibility and possibility of phase change.

2.1. Porous medium deformation and fracture propagation

In this section, we briefly recapitulate the basic notations and the underlying equations of the phase field method for pressurized fractures in brittle materials.

1
2
3
4
5
6
7
8
9 **2.1.1. Variational formulation of brittle fracture**

10 We consider a two-dimensional porous medium under plane strain loading
 11 occupying an open Lipschitz domain $\Omega \subset \mathbb{R}^2$. Let $\Gamma_D, \Gamma_N \subseteq \partial\Omega$ be such that
 12 $\Gamma_D \cup \Gamma_N = \partial\Omega$ and $\Gamma_D \cap \Gamma_N = \emptyset$, and $\mathbf{u}_D : \Gamma_D \rightarrow \mathbb{R}^2$ and $\mathbf{t}_N : \Gamma_N \rightarrow \mathbb{R}^2$ be
 13 prescribed displacement and traction boundary conditions, respectively. Also,
 14 let $\Gamma_B \subset \partial\Omega$ denote the boundary of a borehole. We let $Q_g : \Gamma_B \rightarrow \mathbb{R}$ denote
 15 the fluid source and $\mathbf{b} : \Omega \rightarrow \mathbb{R}^2$ the body force per unit volume exerted to the
 16 solid.
 17



34 Figure 1: Schematic of (a) a sharp fracture and (b) the diffusive phase field profile for the
 35 same fracture. In both figures, a square plate with a borehole placed inside is shown. The *in*
 36 *situ* stress is applied on the external boundary, while the fluid is injected from the boundary
 37 of the borehole. We will only use the diffusive phase field in the proposed method.

38 The variational approach to fracture is built on energy minimization with
 39 respect to the displacement field $\mathbf{u} : \Omega \rightarrow \mathbb{R}^2$ and its jump set, which we denote
 40 as $\mathcal{C} = \mathcal{C}(\mathbf{u}) \subset \Omega$. Let $|\mathcal{C}|$ denote the one-dimensional Hausdorff measure of \mathcal{C} .
 41 Following Griffith's theory, the total potential energy of the fractured poroelastic
 42 solid is written as:
 43

$$\begin{aligned} \Pi_{\mathcal{C}}[\mathbf{u}, \mathcal{C}] := & \int_{\Omega \setminus \mathcal{C}} \psi_0[\varepsilon(\mathbf{u})] d\Omega - \int_{\Omega} \mathbf{b} \cdot \mathbf{u} d\Omega - \int_{\Gamma_N} \mathbf{t}_N \cdot \mathbf{u} d\Gamma \\ & - \int_{\Omega \setminus \mathcal{C}} (\alpha - 1) p \operatorname{div} \mathbf{u} d\Omega + \int_{\Omega \setminus \mathcal{C}} \nabla p \cdot \mathbf{u} d\Omega + g_c |\mathcal{C}|, \end{aligned} \quad (1)$$

49 where p denotes the pore pressure, $\alpha \in [0, 1]$ is the Biot coefficient. Constant
 50 $g_c \in \mathbb{R}^+$ is the strain energy released per unit length of fracture extension. The
 51 strain energy density $\psi_0[\varepsilon(\mathbf{u})]$ is given by
 52

$$\psi_0(\varepsilon) := \frac{\lambda}{2} (\operatorname{tr} \varepsilon)^2 + G \|\varepsilon\|^2,$$

55 with λ and G Lamé constants. These constants are related to Young's modulus
 56 E and Poisson's ratio ν as $\lambda = E\nu / [(1+\nu)(1-2\nu)]$ and $G = E / [2(1+\nu)]$. The
 57
 58
 59

linearized strain tensor takes the form:

$$\boldsymbol{\varepsilon}(\mathbf{u}) := \frac{1}{2} (\nabla \mathbf{u} + \nabla \mathbf{u}^T).$$

Finally, $\|\cdot\|$ denotes the Frobenius norm of a tensor.

2.1.2. Regularized variational formulation of brittle fracture

To develop a numerical method to approximate (1), the phase field approach replaces the sharp-fracture description \mathcal{C} with a phase field description, where the phase field is denoted as $d : \Omega \rightarrow [0, 1]$. In particular, regions with $d = 0$ and $d = 1$ correspond to the intact and fully broken materials, respectively. Using a phase field approach, the one-dimensional fracture \mathcal{C} is approximated with the help of an elliptic functional [29, 30]:

$$\mathcal{C}_\ell[d] := \frac{1}{4c_w} \int_{\Omega} \left(\frac{w(d)}{\ell} + \ell \nabla d \cdot \nabla d \right) d\Omega, \quad (2)$$

where $\ell > 0$ is the regularization length scale, which may also be interpreted as a material property, e.g., the size of the process zone. See Remark 3 for comments on the choice of ℓ . Constant $c_w = \int_0^1 \sqrt{w(d)}$ is a normalization constant such that when $\ell \rightarrow 0$, $\mathcal{C}_\ell[d]$ converges to the length of the sharp fracture, $|\mathcal{C}|$. Classical examples of $w(d)$ and c_w are $w(d) = d^2$ and $c_w = 1/2$ for the AT2 model, and $w(d) = d$ and $c_w = 2/3$ for the AT1 model. Between these models, the AT1 model which is better at simulating crack nucleation [31] predicts a phase field profile with a support of a finite width, but requires solving inequality constrained optimization problems; the AT2 model, which normally requires a pre-existing crack (at least for a homogeneous material under low-speed loading), gives a diffuse phase field profile, but can be implemented as constrained optimization problems which are much easier to solve. Interested readers are referred to [31, 32] for more elaborations. In this paper all numerical examples are implemented with the AT1 model, while we keep our formulation general for both models.

On this basis, we replace (1) by a global constitutive dissipation functional for a rate independent fracture process [33]:

$$\begin{aligned} \Pi[\mathbf{u}, d] := & \int_{\Omega} \psi[\boldsymbol{\varepsilon}(\mathbf{u}), d] d\Omega - \int_{\Omega} \mathbf{b} \cdot \mathbf{u} d\Omega - \int_{\Gamma_N} \mathbf{t}_N \cdot \mathbf{u} d\Gamma \\ & - \int_{\Omega} (1-d)^2 (\alpha - 1) p \operatorname{div} \mathbf{u} d\Omega + \int_{\Omega} (1-d)^2 \nabla p \cdot \mathbf{u} d\Omega \\ & + \frac{g_c}{4c_w} \int_{\Omega} \left(\frac{w(d)}{\ell} + \ell \nabla d \cdot \nabla d \right) d\Omega, \end{aligned} \quad (3)$$

where the admissible sets of displacement and phase field can be set as:

$$\mathcal{S}_u := \{ \mathbf{u} \in H^1(\Omega; \mathbb{R}^2) | \mathbf{u} = \mathbf{u}_D \text{ on } \Gamma_D \}, \quad (4a)$$

$$\mathcal{S}_d := \{ d \in H^1(\Omega) | 0 \leq d \leq 1 \}. \quad (4b)$$

In practice, (4b) will be used in combination with the irreversibility constraint, to be elaborated in Remark 2.

Remark 1 (Strain energy degradation). *The solid endures partial loss of stiffness due to the presence of fractures. In order to model this effect, the strain energy density is degraded with respect to the evolution of the phase field. Also note that as the damaged material responds differently to tension and compression, we let only a part of the strain energy density be degraded. For this purpose, we let the degraded strain energy in (3) take the following general form:*

$$\psi(\boldsymbol{\varepsilon}, d) = g(d)\psi_+ + \psi_-,$$

where $g(d)$ satisfies $g(0) = 1$, $g(1) = 0$, and $g'(d) < 0$ for all d such that $0 \leq d \leq 1$ [17]. A usual choice is $g(d) = (1 - d)^2$. On the other hand, ψ_{\pm} are such that

$$\psi_+(\boldsymbol{\varepsilon}) + \psi_-(\boldsymbol{\varepsilon}) = \psi_0(\boldsymbol{\varepsilon}).$$

Now since $\partial\psi/\partial d = g'(d)\psi_+$, only ψ_+ contributes to fracture propagation.

There are several phase field models that differ in their choice of ψ_{\pm} . In this paper, we adopt the one proposed by Amor *et al.* [34]. This model assumes both volumetric expansion and deviatoric deformation contribute to fracture propagation, but volumetric compression does not. A decomposition of $\boldsymbol{\varepsilon}$ into volumetric and deviatoric parts reads:

$$\text{vol } \boldsymbol{\varepsilon} := \frac{1}{3}(\text{tr } \boldsymbol{\varepsilon})\mathbf{1}, \quad \text{dev } \boldsymbol{\varepsilon} := \boldsymbol{\varepsilon} - \text{vol } \boldsymbol{\varepsilon}.$$

See Appendix A.1 for more details.

Remark 2 (Irreversibility constraint). *The requirement $g'(d) < 0$ comes from the underlying irreversibility condition (the fracture can never heal) in time:*

$$\partial_t d \geq 0. \tag{5}$$

Consequently, modeling of fracture evolution problems leads to inequality constraints, and sometimes gives rise to a variational inequality formulation.

As an alternative way to model the irreversibility, Miehe *et al.* [35] proposed a phase field model based on a local history field. In this model, the evolution of the phase field d is driven by the historically maximum value of ψ_+ at the point of interest.

Remark 3 (The choice of ℓ). *Based on an analytical solution for the critical tensile strength σ_{cr} that a one-dimensional bar can sustain [32], we use the following equation for the choice of ℓ :*

$$\ell = \frac{3Eg_c}{8\sigma_{cr}^2}, \tag{6}$$

where E and g_c can be obtained from regular experiments, while σ_{cr} can be approximated by the tensile strength σ_t . Assuming all other parameters are known, the formula (6) is able to estimate ℓ , though the accuracy is unknown for more complex cases.

1
2
3
4
5
6
7
8
9
10 2.2. Carbon dioxide as a compressible fluid

11 The governing equations for the fluid flow in a porous medium are given by
12 mass conservation, momentum balance, and the equation of state. The mass
13 conservation equation reads:

$$\begin{aligned} \partial_t(\phi\rho) + \nabla \cdot (\rho\mathbf{v}) &= 0 && \text{in } \Omega, \\ -\rho\mathbf{v} \cdot \mathbf{n} &= Q_g && \text{on } \Gamma_B. \end{aligned} \quad (7)$$

17 Here ϕ denotes the porosity of the porous medium (the fraction of volume
18 occupied by the fluid), ρ the density of the fluid, \mathbf{v} the Darcy velocity vector,
19 and Q_g the fluid source. Note that Q_g has the unit of volumetric flow rate per
20 unit volume. Also, we assume the rock is saturated by the fluid so that the fluid
21 content in rock per volume is expressed by $\phi\rho$.
22

23 In addition to (7), we state the momentum balance in the form of Darcy's
24 law. Note that this assumption is for the flow in conventional reservoirs, al-
25 though there are more complicated flow regimes, namely slip flow, transition
26 flow, and Knudsen diffusion, for which Darcy's law in its current form cannot
27 be used. For more details we refer the reader to [36, 37, 38, 39]. Neverthe-
28 less modeling the flow at the microscale is out of the scope of this paper that
29 deals with a continuum formulation, and hence we confine ourselves to Darcy's
30 law throughout this work. This implies a linear relationship between the fluid
31 velocity and the head pressure gradient:
32

$$\mathbf{v} = -\frac{k}{\mu} \nabla p, \quad (8)$$

33 where $k = k(d)$ is the permeability of the rock, and μ is the dynamic fluid
34 viscosity. Note that there could be an additional term $-\rho g \nabla z$ on the right hand
35 side of (8), where g and z are the magnitude of the gravitational acceleration
36 and the depth, respectively. This term is, however, in our case negligible, as
37 we assume an almost horizontal computational domain. Also, we assume the
38 porosity is not dependent on the stress condition.
39

40 On the other hand, we correlate the permeability to the phase field value
41 as it is clear that when the crack starts propagating, the permeability of the
42 solid matrix starts to increase, as the crack width increases. To incorporate
43 this effect into our model, an exponential variation of the fluid permeability has
44 been adopted from [40, 41]:
45

$$k(d) = k_0 \exp(\alpha_k d), \quad (9)$$

46 where k_0 is the permeability of the intact material, and α_k is a coefficient to
47 indicate the effect of phase field evolution on the permeability. We take $\alpha_k = 7.0$
48 according to [41]. In real applications, α_k can be obtained from experiments.
49
50 Figure 2 illustrates the permeability increasing with respect to the evolution of
51 the phase field variable. As seen therein, the permeability starts from an initial
52 value for a completely intact porous medium to a very big value of permeability
53 in the fully broken area.
54

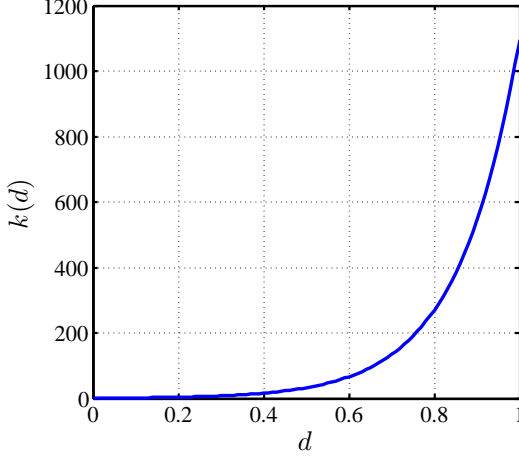


Figure 2: Plot of $k(d) = \exp(7.0d)$, permeability, as a function of the phase field variable d .

The first term on the left hand side of (7), the rate of change of fluid content, can be written as:

$$\partial_t (\phi\rho) = \rho \partial_t \phi + \phi \partial_t \rho = \rho \partial_t \varepsilon_v + \phi \partial_t \rho, \quad (10)$$

where we have assumed the rate of change of pore volume is equal to that of the volumetric strain, which is given by $\varepsilon_v = \nabla \cdot \mathbf{u}$.

Under isothermal conditions, the gas density varies significantly with pressure. This is captured by an equation of state (EOS). One applicable EOS for CO₂ is known as the Span-Wagner (S-W) equation [28] defined in terms of the Helmholtz free energy. The CO₂ density and pressure are related by:

$$p = (1 + \delta\varphi_\delta^r) \rho RT, \quad (11)$$

where R is the universal gas constant, and φ_δ^r is the derivative of the residual part of the full expression of Helmholtz energy φ^r with respect to the reduced density δ , with

$$\begin{aligned} \varphi^r(\delta, \tau) = & \sum_{i=1}^7 n_i \delta^{d_i} \tau^{t_i} + \sum_{i=8}^{34} n_i \delta^{d_i} \tau^{t_i} e^{-\delta^{c_i}} + \sum_{i=35}^{39} n_i \delta^{d_i} \tau^{t_i} e^{-\alpha_i(\delta - \varepsilon_i)^2 - \beta_i(\tau - \gamma_i)^2} \\ & + \sum_{i=40}^{42} n_i \Delta^{b_i} \delta e^{C_i(\delta - 1)^2 - D_i(\tau - 1)^2}, \end{aligned} \quad (12)$$

in which

$$\Delta = \left\{ (1 - \tau) + A_i \left[(\delta - 1)^2 \right] \frac{1}{2\beta_i} \right\}^2 + B_i \left[(\delta - 1)^2 \right]^{a_i}.$$

In (12), ρ_c and T_c are the critical density and temperature, respectively, and $\delta = \rho/\rho_c$ and $\tau = T/T_c$ are the reduced ones. For the sake of brevity, here we do not provide the definitions and values of other parameters in (12), but refer the readers to [28].

By substituting (8),(9), (10), and (11) in (7), the governing equation for CO₂ flow is written as follows:

$$\begin{aligned} \phi \partial_t \rho + \rho \partial_t \varepsilon_v - \nabla \cdot \left(\rho \frac{k(d)}{\mu} \nabla p \right) &= 0, \quad \text{in } \Omega, \\ \rho \mathbf{v} \cdot \mathbf{n} &= -Q_g, \quad \text{on } \Gamma_B, \\ p &= p_D, \quad \text{on } \Gamma_P, \end{aligned} \tag{13}$$

where $\Gamma_P = \partial\Omega \setminus \Gamma_B$.

Summary of governing equations. The governing equations for modeling the CO₂ fracturing are summarized as follow: for the porous medium deformation, the functional defined in (3) is minimized among $(\mathbf{u}, d) \in \mathcal{S}_u \times \mathcal{S}_d$ under the constraint (5), while for the compressible fluid the boundary value problem (13) is used to solve for the pressure p .

Advantages and limitations of the method. The main advantage of the current approach is its convenience in simulating complex fracture processes, including crack initiation, propagation and merging. In fact, the evolution of fracture surfaces is the natural outcome of the solution of a coupled system of partial differential equations. Such a model significantly decreases the implementation difficulty by avoiding tracking the fracture geometry. In this work, taking advantage of the phase field approach, we consider CO₂ as a compressible fracturing fluid under an isothermal condition. Nevertheless, as this work is the first of its kind, herein a relatively simple model is used for the calculation of gas flow and permeability in shale media.

3. Numerical solution

In this section we present an algorithm that adopts standard procedures to obtain a numerical method to solve the initial boundary value problem presented in Section 2. In this algorithm, a staggered approach is employed to solve the underlying equations, i.e., the solution is obtained via iteration between the variables [17, 42]. This idea is based on the fact that by fixing two variables, the problem becomes convex in the remaining unknown. However, one drawback for such an approach is that it might need many iterations to achieve convergence among the three fields.

For the problem at hand, we need to solve a coupled system consisting of mass balance for the compressible fluid and a dissipative potential energy with the phase field. We provide a fully iterative approach in which at each stage we solve for one unknown while the other two variables are fixed to their values at

Algorithm 1: Algorithm for modeling the CO₂ by phase field.

```
22     Input:  $p_0, d_0, \mathbf{u}_0, \rho_0$ , and  $\varepsilon_{\text{tol}}$ 
23     Output:  $p_n, d_n$ , and  $\mathbf{u}_n, n = 1, \dots, N$ 
24     1 Set flow and mechanical boundary conditions  $\sigma_1, \sigma_3$ , and  $Q_g$ ;
25     2 for  $n = 1$  to  $N$ ; do
26         3     Set  $t = n\Delta t$  and  $k = 0$ ; /*  $k$  is an iteration counter */ *
27         4     repeat
28             5      $m = 0$ ; /*  $m$  is another iteration counter */ *
29             6     repeat
30                 7     Step - P: compute  $p_n$  with (A.6);
31                 8     Step - U: compute  $\mathbf{u}_n$  with (A.1);
32                 9     Update  $\rho_n^{(k+1)} \leftarrow \rho(p_n^{(k)})$  with (11);
33                 10     $k + 1 \leftarrow k$ 
34                 11    until  $\|p_n^{(k)} - p_n^{(k-1)}\|_2 < \varepsilon_{\text{tol}}$  and  $\|\mathbf{u}_n^{(k)} - \mathbf{u}_n^{(k-1)}\|_2 < \varepsilon_{\text{tol}}$ ;
35                 12    Step - d: compute  $d_n$  with (A.1);
36                 13     $m + 1 \leftarrow m$ 
37                 14    until  $\varepsilon_d = \|d_n^{(m)} - d_n^{(m-1)}\|_2 < \varepsilon_{\text{tol}}$ ;
38                 15     $\mathbf{u}_{n-1} \leftarrow \mathbf{u}_n$ ;
39                 16     $p_{n-1} \leftarrow p_n$ ;
40                 17     $\rho_{n-1} \leftarrow \rho_n$ ;
41         18 end
```

the last iteration. Readers are referred to Algorithm 1 for complete elaboration.

[An alternative algorithm is the fixed-stress split, see \[43, 44\].](#)

We implement our method on FEniCS, an open-source finite element software [45, pp. 173–225]. Therein, the user merely needs to provide the variational form of the problem as well as the geometry and mesh information. Then, a big advantage of FEniCS is that the software itself completes all steps toward generating the global stiffness matrix.

Below we show an excerpt of the used FEniCS code. This piece of code performs some calculations for line 8 in Algorithm 1 wherein \mathbf{u} is solved for while the other two unknowns are fixed. It first defines $\boldsymbol{\varepsilon}$, ψ_0 , and $\psi(\boldsymbol{\varepsilon}, d)$ in lines 1, 3, and 5, respectively. Then, the standard finite element shape functions are defined in line 8, and the admissible function space (`TrialFunction`), the test function space (`TestFunction`), and the unknown function \mathbf{u} (`Function`) are defined in line 9. Afterwards, the elastic energy is introduced as a variational form in line 11. Finally, in lines 12 and 13, the code takes the first variation $\delta\Pi[(\mathbf{u}, d); \bar{\mathbf{u}}]$ (A.1a) and the second variation $\delta^2\Pi[(\mathbf{u}, d); \bar{\mathbf{u}}; \delta\mathbf{u}]$ (A.2a) and builds the nodal residual vector as `Residual_u` and the tangent stiffness matrix as `Jacobian_u`.

```

1 def eps(u_):
2     return sym(grad(u_))
3
4 def psi_0(u_):
5     return 0.5 * lmbda * tr(eps(u_))**2 + mu * eps(u_)**2
6 def psi_(u_, d_):
7     return ((1 - d_)**2 + k_ell) * psi_0(u_)
8
9 V_u = VectorFunctionSpace(mesh, "CG", 1)
10 u_, u, u_t = Function(V_u), TrialFunction(V_u), TestFunction(V_u)
11 energy_elastic = psi_(u_, d_) * dx
12 Residual_u = derivative(energy_elastic, u, u_t)
13 Jacobian_u = derivative(Residual, u_, u_t)

```

To solve the three unknowns, we select for \mathbf{u} and p the linear solver MUMPS which is convenient for solving large linear systems [46], and for d the TAO optimization solver integrated into the PETSc library [47, 48], which has the capability of solving inequality constrained optimization problems as the one at hand. Interested readers are referred to [49] for more information about the applied solvers.

4. Numerical examples

In this section, we present a set of numerical examples to demonstrate the capability of the proposed model. First, we aim to verify our implementation of the present phase field method for CO₂ fracturing. To this end, we present three examples with exact or otherwise well-established solutions to verify our

outputs. Next, we present three more numerical example to demonstrate the capability of the proposed model.

We also refer the interested readers to Wilson and Landis [50] and Chukwudzie [43] in which the phase field approach to hydraulic fracturing is verified with classical two-dimensional analytical solutions [51, 52].

4.1. Single-edge-notched tension test

First, following an example motivated by Miehe *et al.* [53], we investigate a square plate with a horizontal initial crack at the middle height starting from the left end and ending at the plate center. The geometric setup is depicted in Figure 10. To capture the crack pattern properly, the mesh is refined in areas where the crack is expected to propagate, i.e., in the center strip of the specimen. In effect, for a discretization with 105,352 standard P_1 elements, an effective element size of $h \approx 5 \times 10^{-3}$ mm is obtained in the critical zone. The specimen is under a direct tension test, in which a monotonically increasing displacement with constant increments $\Delta u = 6 \times 10^{-5}$ mm is imposed on the top edge while the bottom edge is fixed. In this example, the evolution is simulated for 100 uniform time steps so that a final deformation of 6×10^{-3} mm is reached. We will adopt the values of the material parameters given in Table 1.

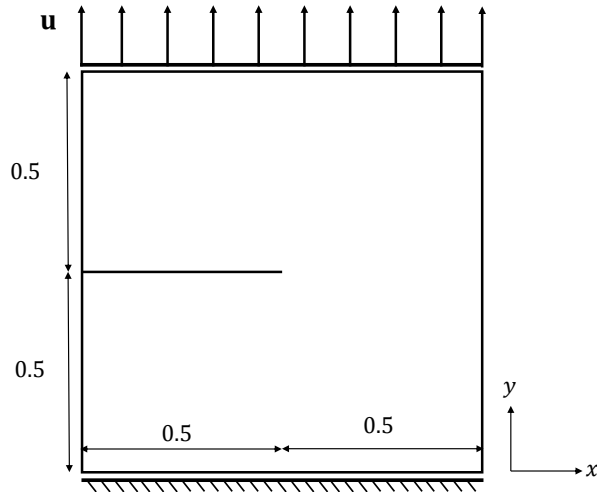


Figure 3: Schematic of a cracked square plate (unit: mm) under a single-edge-notched tension test. A monotonically increasing displacement with constant increments $\Delta u = 6 \times 10^{-5}$ mm is applied on the top edge while the bottom edge is fixed.

The resulting crack patterns at different stages of the deformation for two fixed regularization length scales $\ell = \ell_1 = 1 \times 10^{-2}$ mm and $\ell = \ell_2 = 2 \times 10^{-2}$ mm are illustrated in Figure 4. As expected, in both simulations, the fracture propagates straightforward to the end. This straight crack topology agrees well with the results in [55]. Also as seen, the resulting crack pattern with the smaller ℓ looks sharper.

1
2
3
4
5
6
7
8
9 Table 1: Cracked square plate under a tension test: Material parameters [54]

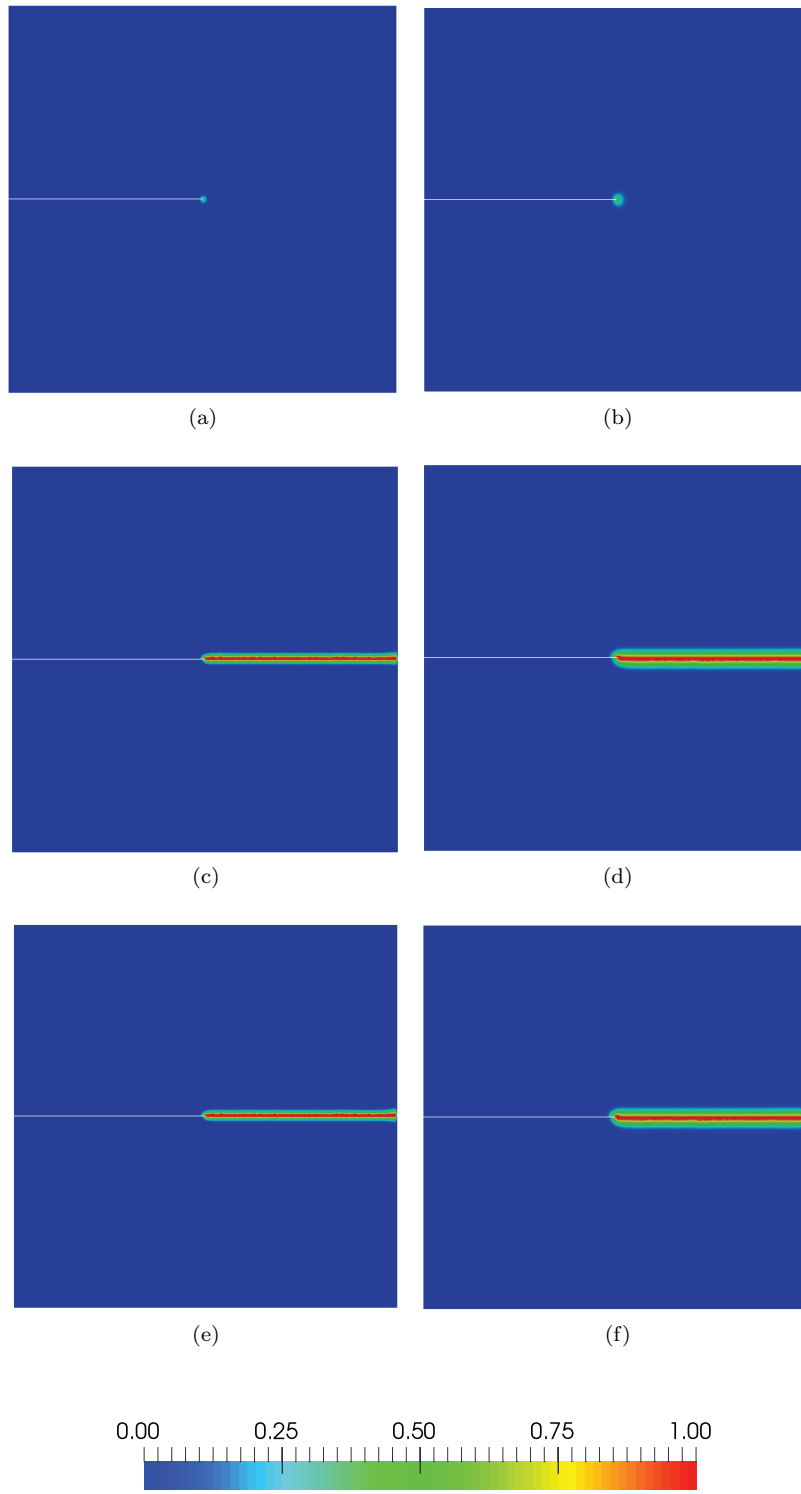
10
11
12
13
14

Parameters	symbol	unit	value
Young's modulus	E	MPa	210×10^3
Poisson's ratio	ν	—	0.3
Critical energy release rate	g_c	MPa·mm	2.7

15
16
17
18
19
20
21
22
23
24
25
26
27
28
29
30
31
32
33
34
35
36
37
38
39
40
41
42
43
44
45
46
47
48
49
50
51
52
53
54
55
56
57
58
59
60
61
62
63
64
65

We also output the load-deflection curves for the two setups of Figure 5. As seen, both models will result in similar trends. Hence, the effect of ℓ on the response is small in this range.

1
2
3
4
5
6
7
8
9
10
11
12
13
14
15
16
17
18
19
20
21
22
23
24
25
26
27
28
29
30
31
32
33
34
35
36
37
38
39
40
41
42
43
44
45
46
47
48
49
50
51
52
53
54
55
56
57
58
59
60
61
62
63
64
65



14

Figure 4: Cracked square plate under a tension test with two different regularization length scales $\ell = \ell_1 = 10^{-2}$ mm $\approx 2h$ (left) and $\ell = \ell_2 = 2 \times 10^{-2}$ mm $\approx 4h$ (right). Both simulations are done with 100 uniform time steps with $\Delta u = 6 \times 10^{-5}$ mm (See also Table 1 for the input values). Phase field contours at three different stages $u = 5.52 \times 10^{-3}$ mm (4a,4b), $u = 5.58 \times 10^{-3}$ mm (4c,4d), and $u = 6 \times 10^{-3}$ mm (4e,4f) are shown in deformed configurations with the deformations scaled. The initial cracks are explicitly imposed, so in the deformed configuration it appears as a white line. As expected, we observe a straight crack pattern in both cases.

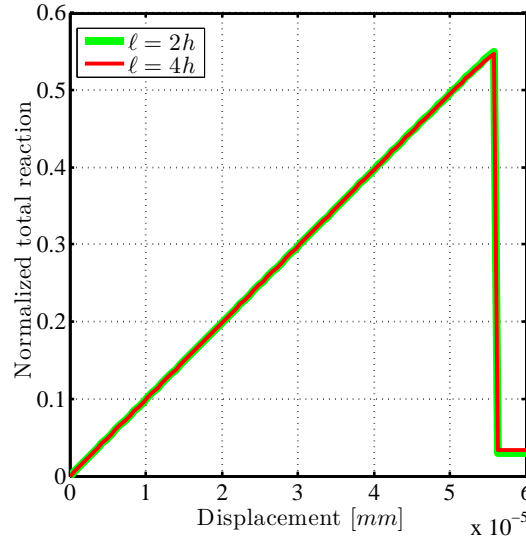


Figure 5: Cracked square plate under a tension test with two different regularization length scales $\ell = \ell_1 = 10^{-2}$ mm $\approx 2h$ (red) and $\ell = \ell_2 = 2 \times 10^{-2}$ mm $\approx 4h$ (green). Load-deflection curves for both ℓ_1 and ℓ_2 are obtained. Both simulations are done with 100 load steps with $\Delta u = 6 \times 10^{-5}$ mm. The total reaction is normalized by the one in the case without any crack or phase field evolution. Both models give rise to similar trends so the effect of changes in ℓ is small within this range. Note that the reaction highly decreases at the 93rd time step where the crack starts to propagate.

1
2
3
4
5
6
7
8
9
10
11
12
13
14
15
16
17
18
19
20
21
22
23
24
25
26
27
28
29
30
31
32
33
34
35
36
37
38
39
40
41
42
43
44
45
46
47
48
49
50
51
52
53
54
55
56
57
58
59
60
61
62
63
64
65

265 4.2. *Poroelastic response of a borehole*

This example aims to study the effect of fluid pressurization on the poroelastic response around the borehole. It was first studied by Detourney and Cheng [56] (see also [11, 57]). Consider a plane strain hydraulic fracturing problem where there is a square plate containing a central borehole. The geometry and the loading conditions in this example are the same as Figure 12. The far-field *in situ* stress is set to zero in this example. Note also that $d \equiv 0$, i.e., there is no preexisting crack in the specimen and we do not allow for any nucleation of the fracture as the rock strength is assigned a very large value. A discretization with 28,140 standard P_1 elements is applied to the problem. To capture the high gradient of pressure near the borehole, the mesh is refined in that area so that an effective mesh size of $h \approx 0.15$ mm is adopted. The fluid is slightly compressible, and we set the fluid pressure in the borehole to 1 MPa. The other material properties are prescribed according to Table 2.

Here, the governing equation for the slightly compressible flow is written as follows [56]:

$$\partial_t p + M \nabla \cdot \left(\frac{k_0}{\mu} \nabla p \right) = 0$$

where $M = E(1-\nu)/[(1+\nu)(1-2\nu)]$ is called the constrained modulus.

Table 2: Poroelastic response of a borehole: Material parameters

Parameters	symbol	unit	value
Young's modulus	E	MPa	6000
Poisson's ratio	ν	—	0.34
Biot coefficient	α	—	1.
Permeability	k_0	mm^2	1×10^{-12}

280 Figure 6 shows the distribution of pore pressure around the borehole for three values of dynamic viscosity μ at early time $t = 0.1$ s. Note that the horizontal axis is $(r - r_0)/r_0$, ranging from 0 to 0.25 in the direction of $\theta = \pi/2$. The simulation results are then compared to the analytical solution by Detourney and Cheng [56].

285 Figure 7 depicts the effect of dynamic viscosity on the effective tangential stress in the vicinity of the borehole at early time $t = 0.1$ s.

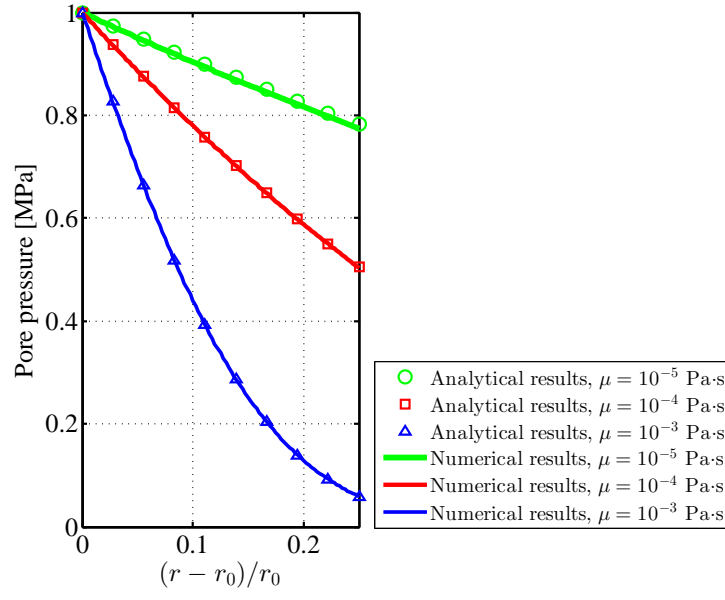


Figure 6: Poroelastic response of a borehole. The distribution of pore pressure caused by fluid pressurization is shown around the borehole for three different dynamic viscosities μ at early time $t = 0.1$ s. As seen, the results are in good accordance with the analytical in [56].

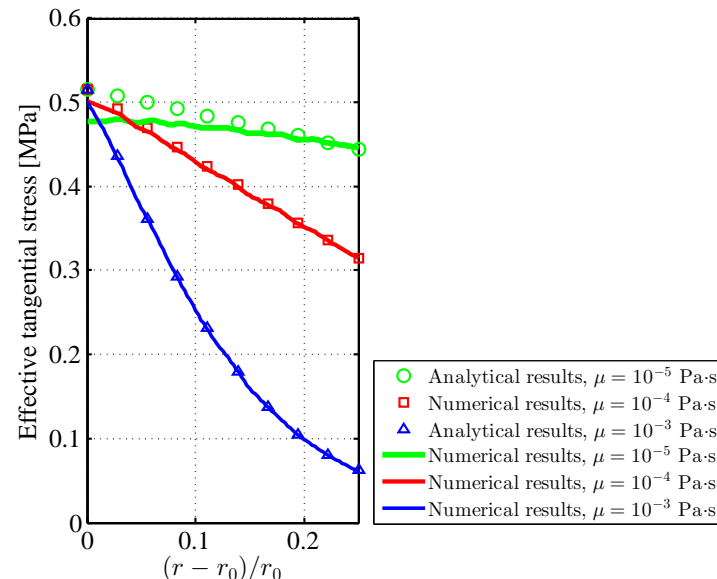


Figure 7: Poroelastic response of a borehole. The effective tangential stress is plotted near the borehole for three different dynamic viscosities μ at early time $t = 0.1$ s.

1
2
3
4
5
6
7
8
9 *4.3. Computation of the crack opening displacement*

10 We now focus on a classical problem first solved by Sneddon and Lowengrub
11 [58] (see also [20]) that solves the opening displacement of a static line crack.

12 Consider a computational domain of $\Omega = 4 \text{ m} \times 4 \text{ m}$ with a preexisting line
13 fracture of length $2a_0 = 0.4 \text{ m}$, i.e., $\mathcal{C} = [1.8, 2.2] \times \{0\}$. To minimize the effect
14 of the boundary conditions on the results, the domain size is much larger than
15 the crack length ($L \gg 2a_0$).

16 The mechanical properties of the material are the Young's modulus $E = 1000$
17 MPa, the Poisson's ratio $\nu = 0$, and the fracture toughness $g_c = 1 \text{ MPa}\cdot\text{s}$.

18 We impose zero displacements on the external boundary of Ω . Also we set
19 $d = 1$ on prescribed (initial) fracture and $d = 0$ on the external boundary of
20 Ω . A monotonically increasing pressure is applied on the upper and lower faces
21 of fracture with the magnitude $p = 1 \text{ MPa}$. Figure 8 depicts the geometry and
22 boundary conditions.

23 Bourdin *et al.* [33] proposed a formula to compute the fracture aperture as:

$$w = \mathbf{u} \cdot \mathbf{n}_\Gamma \simeq \int_s \mathbf{u} \cdot \nabla d \, dx.$$

24
25
26
27
28 Then, the fracture volume is calculated by integrating the fracture aperture
29 along the fracture's path:

$$V_f = \int_\Gamma w \, ds \simeq \int_\Omega \mathbf{u} \cdot \nabla d \, d\Omega.$$

30
31 Figure 9 shows the aperture profile for different h and ℓ . The dash line in
32 black represents the Sneddon's analytical solution [58]. Also, the crack volume
33 computed by Sneddon's analytical solution and our numerical tests are summa-
34 rized in Table 3.

52 Table 3: Crack volumes for different ℓ for numerical tests and analytical solution ($h = 4\text{mm}$).

ℓ (mm)	1.4×10^2	1.2×10^2	1.0×10^2
Numerical fracture volume (mm^2)	2.89×10^2	2.75×10^2	2.60×10^2
Analytical fracture volume (mm^2)	2.51×10^2		

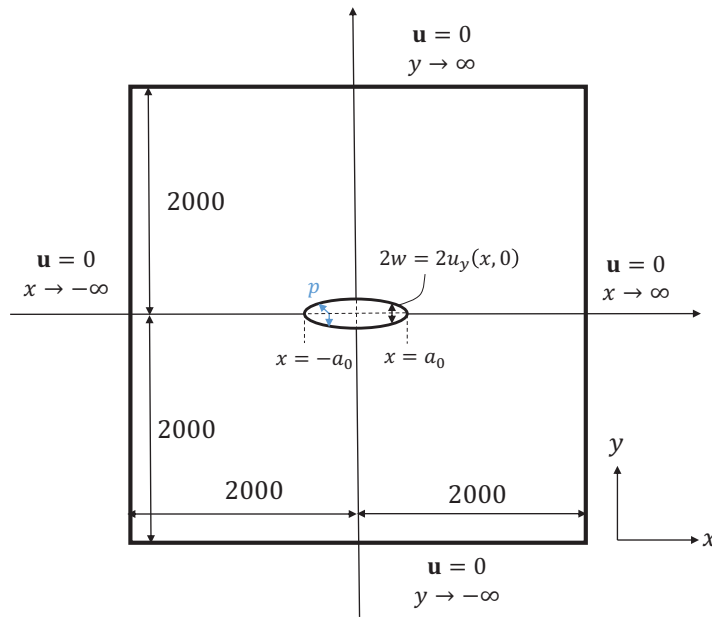


Figure 8: Computation of the crack opening displacement. Schematic view of the deformed line crack in a two dimensional domain.

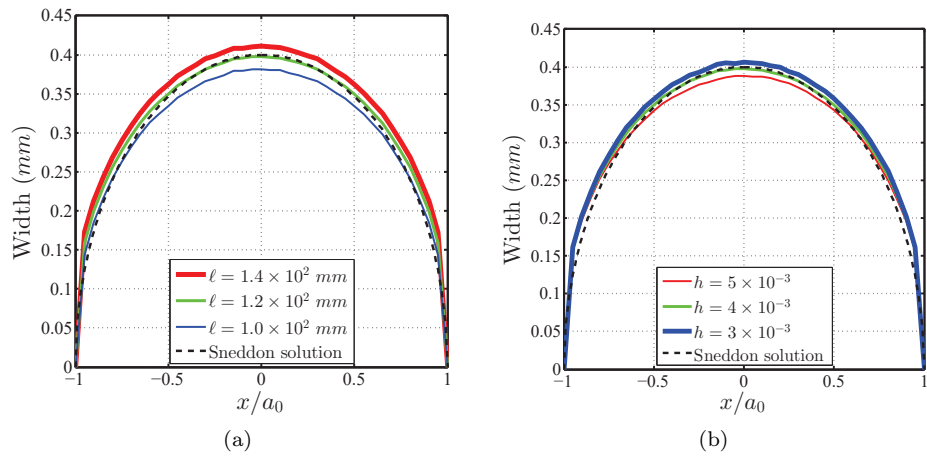
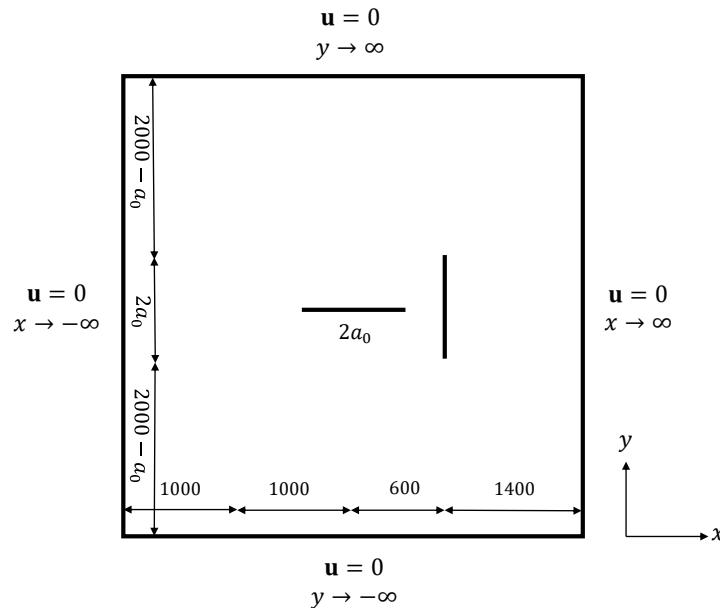


Figure 9: Computation of the crack opening displacement. We output the results for (9a) various ℓ with $h = 4$ mm and (9b) various h with $\ell = 1.2 \times 10^2$ mm, and compare them with Sneddon's analytical solution [58].

1
2
3
4
5
6
7
8
9 4.4. Increasing pressure leading to joining fractures

10 This example motivated by Wheeler *et al.* [59] demonstrates one major capability
11 of the phase field approach that there is no need to track any complicated
12 fracture geometry for joining fractures.

13 Consider a computational domain of $\Omega = (0, 4.0) \times (0, 4.0)$ (unit: m by m)
14 containing two pre-existing line fractures with a length of $2a_0 = 0.4$ m, more
15 precisely, $\mathcal{C}_h = [1.8, 2.2] \times \{0\}$ and $\mathcal{C}_v = \{2.6\} \times [1.8, 2.2]$. To minimize the
16 effect of the boundary conditions on the results, the domain size is much bigger
17 than the fracture length ($L \gg 2a_0$). A discretization with 19,368 standard P_1
18 elements is applied such that an effective element size of $h \approx 20$ mm is obtained
19 in the critical zone. Also, let $\ell = 2h$. Figure 10 depicts the geometric setup.
20 A zero displacement is imposed on the boundary. Also, we set $d = 1$ for the
21 prescribed (initial) fractures, and $d = 0$ on the boundary. A monotonically
22 increasing pressure is applied on the upper and lower faces of the fracture with
23 the magnitude $p = m\bar{p}$ where $\bar{p} = 0.01$ MPa and $m = 1, 2, \dots, 115$.



47 Figure 10: Schematic of a square plate (unit: mm) with two pre-existing fractures. A monotonically
48 increasing pressure with constant increments $p = m\bar{p}$ is applied on the fracture faces.

49 Following [59], we adopt the values of the material parameters given in Table
50 320 4.

51 Figure 11 shows the phase field evolution at different load steps: (11a) $m = 1$,
52 (11b) $m = 113$, (11c) $m = 114$, and (11d) $m = 115$. The results show that the
53 horizontal fracture starts to propagate at $m = 113$, and at $m = 114$ it intersects
54 the vertical fracture. Overall speaking the fracture paths agree with those in
55 [59]. Note the fracture propagation is unstable in this example.

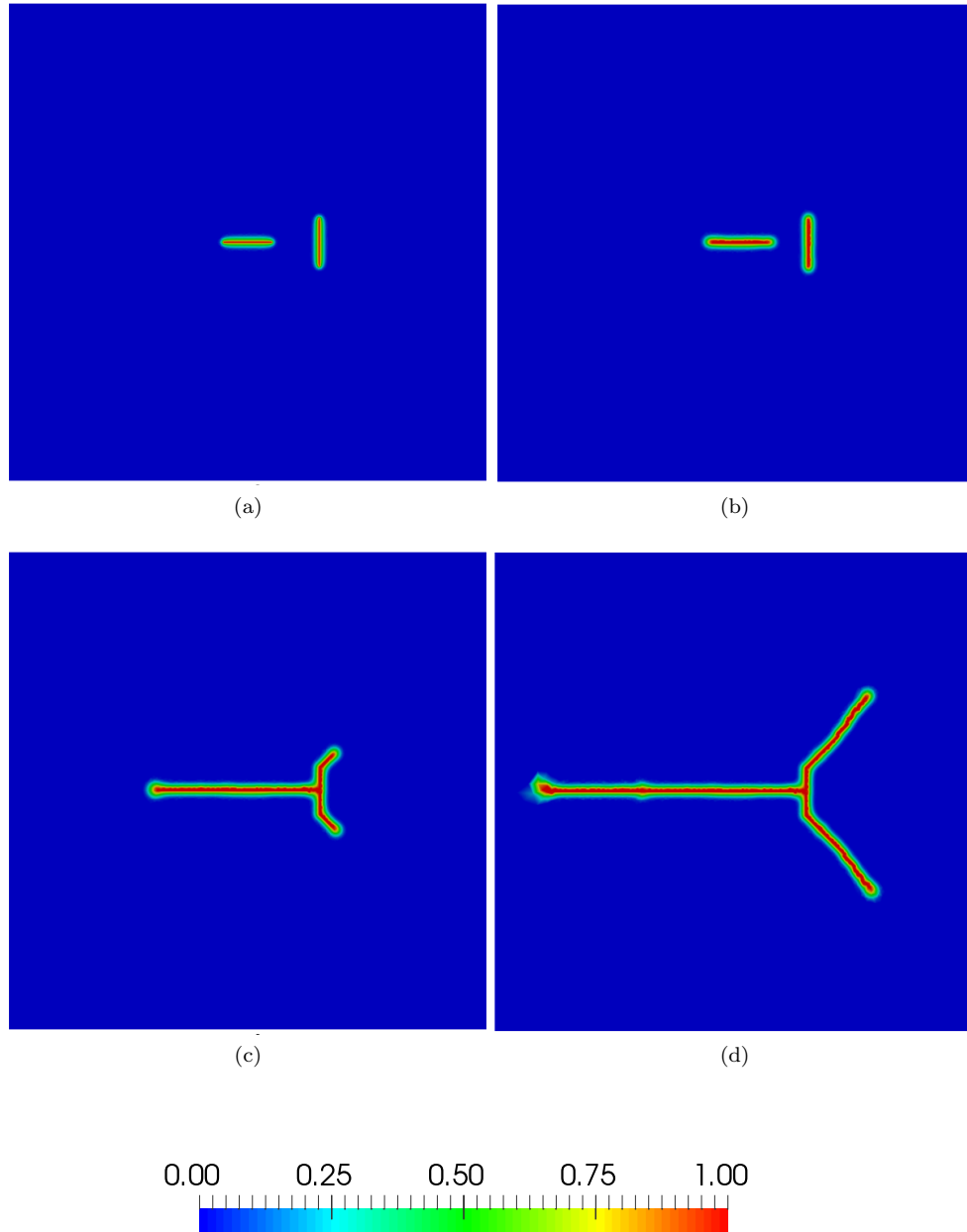


Figure 11: Increasing pressure leading to joining fractures ($p = m\bar{p}$). Phase field contours at different load steps (11a) $m = 1$, (11b) $m = 113$, (11c) $m = 114$, and (11d) $m = 115$. The results show that the horizontal fracture starts to propagate at $m = 113$, and at $m = 114$ it intersects the vertical fracture.

Table 4: Increasing pressure leading to joining fractures: Material parameters [59]

Parameters	symbol	unit	value
Young's modulus	E	MPa	1.0
Poisson's ratio	ν	—	0.2
Critical energy release rate	g_c	MPa·mm	1.0

4.5. CO_2 -driven fracture

In this example, we investigate the fracture propagation in a square plate with a pressurized CO_2 flow, with [10, 11] as the benchmarks. The specimen has edge lengths of $L = 170$ mm. The geometric setup and boundary conditions are depicted in Figure 12. The sample is discretized into 4,832 three-noded triangular elements so that the mesh size $h \approx 5.68$ mm is obtained. Also, we set $\ell = 1.6$ mm. Table 5 shows the remaining parameters to be input.

$$\mathbf{u} = \mathbf{u}_D, p = p_D$$

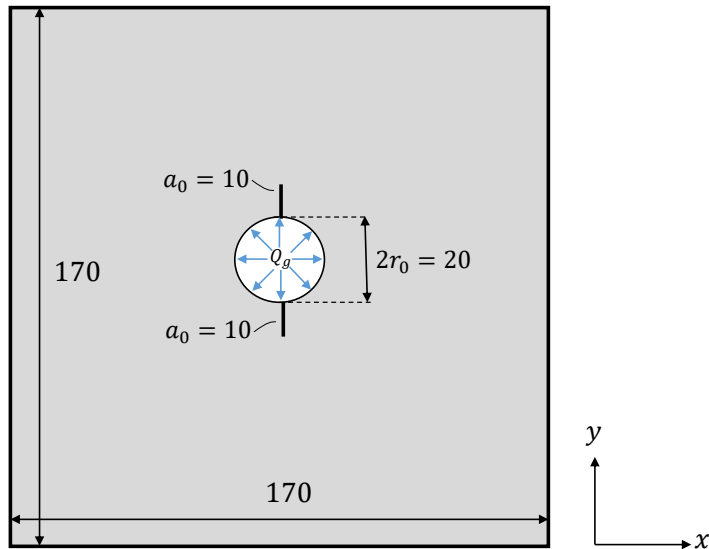


Figure 12: Schematic of a fractured square plate (unit: mm) with pressurized CO_2 flow.

As in Figure 12, there exist two preexisting fractures representing the perforations. We set $d = 1$ for both fractures and set the Dirichlet boundary condition $d = 0$ on the external boundary. The fluid is continuously injected into the central borehole with diameter $2r_0 = 20$ mm, until after the fractures propagate. Note that in this problem, the isothermal condition is adopted so that CO_2 is in the supercritical phase ($T = 45^\circ C$).

For the sake of simplicity, the *in situ* stress $\sigma_1 = \sigma_3 = 1$ MPa is imposed on the boundary by means of its “equivalent” prescribed displacement. More precisely, the displacement of the same specimen with no fracture under the

same *in situ* stress is first computed, then used as the Dirichlet boundary condition for the problem at hand. On the external boundary, we set $p = p_D$ where $p_D = 0$. Moreover, $\Gamma_P = \Gamma_D$ in this example.

Table 5: Default parameter values for the example. These values are taken from [11] except g_c , which is from (6).

Parameters	symbol	unit	value
Young's modulus	E	MPa	6×10^3
Poisson's ratio	ν	—	0.34
Critical energy release rate	g_c	MPa·mm	0.306
Biot coefficient	α	—	0.85
Porosity	ϕ	—	0.01
Initial permeability	k_0	mm ²	1×10^{-12}
Dynamic viscosity of CO ₂	μ	MPa·s	4.04×10^{-11}
Initial pressure	p_0	MPa	0.1
Rock's tensile strength	σ_T	MPa	11

Figure 13 shows the evolution of phase field diagram (left) and pressure profile (right) at different time steps. As seen, the fractures propagate along a straight line, and the pressure profile is accordingly distributed with the highest gradient around the borehole.

Next, we aim to calculate the breakdown pressure p_b , the pressure value when the fractures start to propagate. Figure 14 illustrates the pressure evolution at the top of the borehole and the fracture length function. To estimate the breakdown pressure, first we output the fracture length with regard to (2). Then, we obtain the time when the slope suddenly changes in the fracture length function (\mathcal{C}_ℓ), which is the time corresponding to the breakdown pressure (here $t \approx 0.72t_f$). Hence the breakdown pressure reads $p_b = 10.9$ MPa. This value for p_b is in agreement with H-F and H-W analytical solutions. Also, our results agree with experiments results of Ishida *et al.* [9] within 30%, see Table 6 and the next paragraph for more elaborations.

Table 6: Breakdown pressure of numerical test and analytical solutions for $\sigma_1 = \sigma_3 = 1$ MPa.

	Numerical	H-F solution	H-W solution	Experimental [9]
p_b (MPa)	10.9	11	9.1	8.44

Classical solutions of breakdown pressure. There exist two classical expressions to calculate the breakdown pressure. In the case without poroelastic effect the rock deformation does not penetrate into the pressurized fracture, the Hubbert-Willis (H-W) solution applies [60]:

$$p_b = 3\sigma_3 - \sigma_1 + \sigma_T,$$

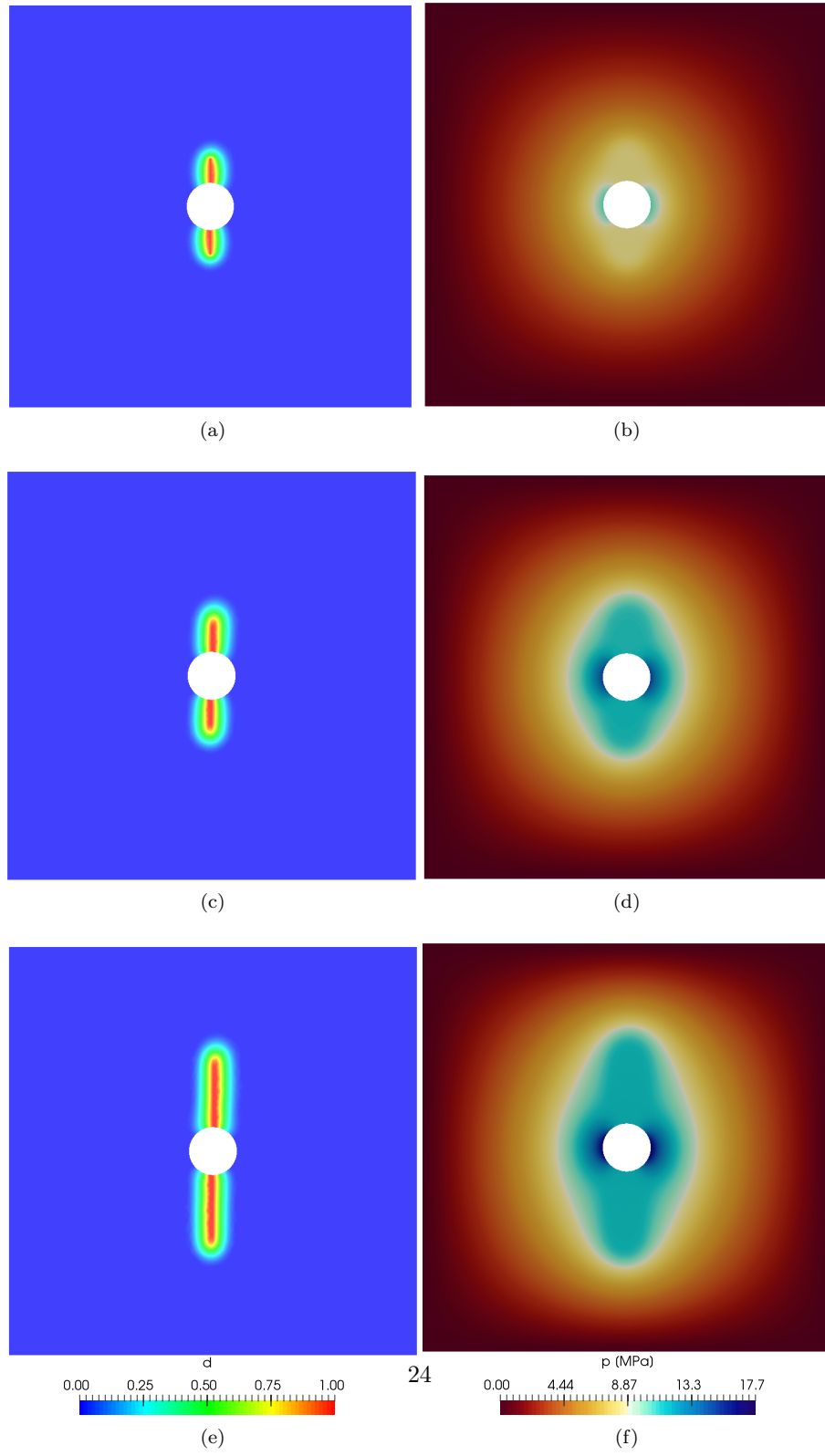


Figure 13: Left: Phase field diagram at different stages (13a) $t = 0.5t_f$, (13c) $t = 0.74t_f$, and (13e) $t = t_f$. Right: Pressure profile at (13b) $t = 0.5t_f$, (13d) $t = 0.74t_f$, and (13f) $t = t_f$.

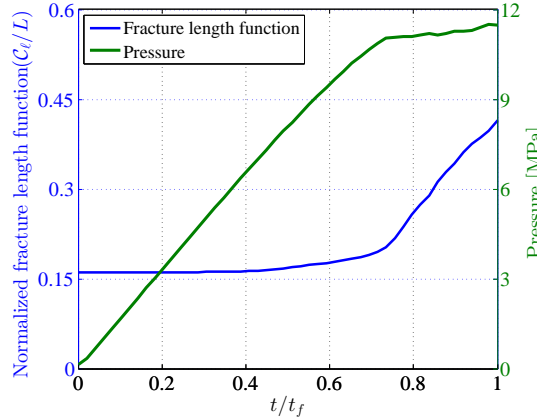


Figure 14: The pressure at the top of the borehole (green line), and the fracture length function (blue line) as functions of time. The time when there is a sudden change of slope in C_ℓ assumes the time corresponding to the breakdown pressure ($t = 0.72t_f$) and the corresponding breakdown pressure is $p_b = 10.9$ MPa. This is in agreement with H-F and H-W analytical solutions.

in which the rock is assumed to be an elastic medium. When the porous medium is set, the Haimson-Fairhurst (H-F) solution is preferred [61]:

$$p_b = \frac{3\sigma_3 - \sigma_1 + \sigma_T + p_0}{1 + \frac{\nu}{1-\nu}\alpha},$$

where we denote by p_b the breakdown fluid pressure, σ_3 , and σ_1 are the minimum and maximum principal stresses, respectively, and σ_T is the rock's tensile strength.

Effect of N , h , and ℓ on the breakdown pressure. Here we aim to study how the number of time steps N , the mesh size h , and the regularization length scale ℓ affect the value of breakdown pressure. As seen in Figure 15, the plots show similar numerical results for the pressure evolution.

Breakdown pressure result of an anisotropic in situ stress. In this example we set the maximum ($\sigma_1 = 3$ MPa) and minimum ($\sigma_3 = 2$ MPa) *in situ* stress. The other input data and boundary conditions are the same as aforementioned.

The pressure at the top of the borehole and the fracture length function, (2), at different stages are illustrated in Figure 16. The breakdown time ($t \approx 0.77t_f$) and the corresponding breakdown pressure is $p_b = 11.9$ MPa, see Table 7.

Table 7: Breakdown pressure of numerical test and analytical solutions for $\sigma_1 = 3$ MPa and $\sigma_3 = 2$ MPa.

	Numerical	H-F solution	H-W solution
p_b (MPa)	11.9	14	9.8

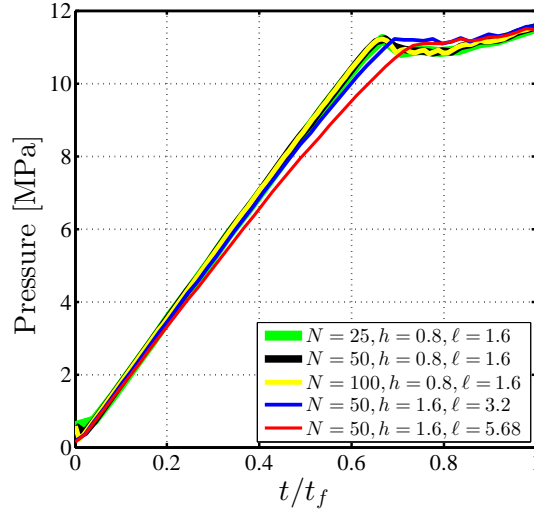


Figure 15: Evolution of the pressure at the top of the borehole for different numbers of time steps N , mesh size h , and ℓ .

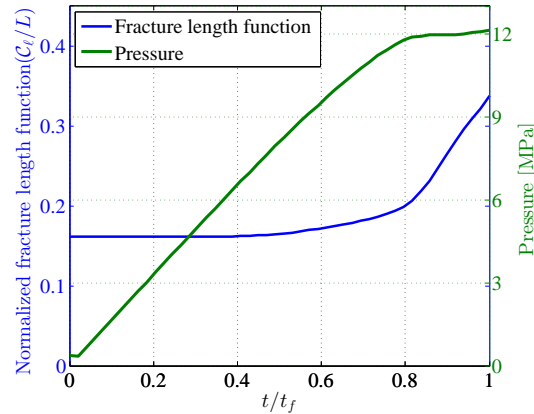


Figure 16: The pressure at the top of the borehole (green line) and the fracture length function (blue line) versus time for deviatoric *in situ* stress are shown. The time ($t \approx 0.8t_f$) when there is a change of slope in the fracture length function (C_ℓ) should correspond to the breakdown pressure ($p_b = 11.9$ MPa).

1
 2
 3
 4
 5
 6
 7
 8
 9
 10
 11
 12
 13
 14
 15
 16
 17
 18
 19
 20
 21
 22
 23
 24
 25
 26
 27
 28
 29
 30
 31
 32
 33
 34
 35
 36
 37
 38
 39
 40
 41
 42
 43
 44
 45
 46
 47
 48
 49
 50
 51
 52
 53
 54
 55
 56
 57
 58
 59
 60
 61
 62
 63
 64
 65

Effect of dynamic viscosity on breakdown pressure. We conduct several numerical examples to investigate the effect of dynamic viscosity μ on the breakdown pressure p_b . In this set of examples an effective mesh size, the mesh size near the borehole or the fractures, $h \approx 1.6$ mm is adopted. Also, we set $\ell = 2h$. In Figure 17 we plot the pressure evolution up to the time when $\mathcal{C}_\ell(t)$ changes slope, so that the end points correspond to the breakdown pressures. The results indicate that p_b is approximately the same for different fluid viscosities, but the time when breakdown pressure reaches is different. Figure 17 demonstrates that the rock will break earlier for the fluid with bigger dynamic viscosity. Also it shows that regardless of the fracturing fluid, the breakdown pressure is slightly the same for all cases. This is in accordance with the physics that the breakdown pressure normally reflects the strength of the solid. However, Wang *et al.* [11] reported different breakdown pressures for different fluids which also agrees with some experiments [9, 10]. We believe this discrepancy demands further research.

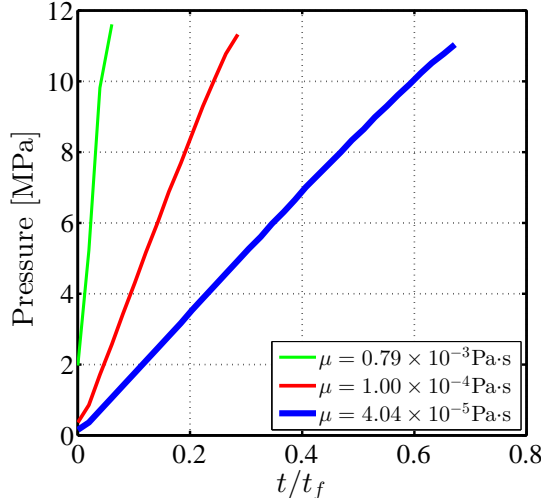


Figure 17: Evolution of the pressure at the top of the borehole for different μ 's. As seen, even though p_b is the same for different fracturing fluids, by increasing μ , the breakdown pressure is reached earlier.

4.6. Interaction between CO₂-driven fractures and natural fractures

In this example, we investigate the interaction between two CO₂-driven fractures and two inclined natural fractures. The specimen has edge lengths of $L = 170$ mm. The geometric setup and boundary conditions are depicted in Figure 18. The sample is discretized into 32,736 three-noded triangular elements so that the mesh size $h \approx 6.25 \times 10^{-1}$ mm is obtained. Also, we set $\ell = 4h$. The remaining input data can be found in Table 5.

As in Figure 18, there exist two pre-existing vertical fractures representing the perforations and two inclined natural fractures. We set $d = 1$ for both initial and inclined natural fractures, and the Dirichlet boundary condition $d = 0$ is

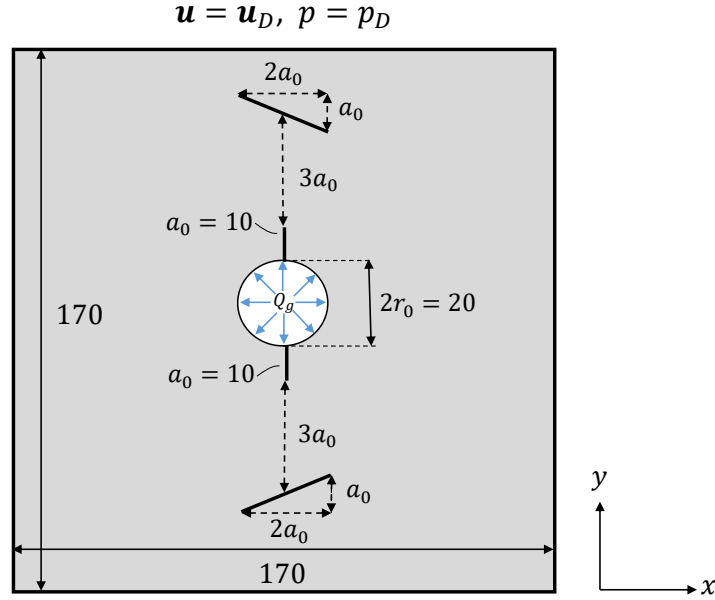


Figure 18: Interaction between CO₂-driven fracture and inclined natural fractures. The geometric setup and boundary conditions are shown (unit: mm). There exist two CO₂-driven fractures and two inclined natural ones.

imposed on the external boundaries. The fluid is continuously injected into the central borehole with diameter $2r_0 = 20$ mm. The *in situ* stress with the value of $\sigma_1 = \sigma_3 = 1$ MPa is also imposed on the boundary by means of its ‘equivalent’ prescribed displacement. See Section 4.5 for more descriptions.

Figure 19 shows the evolution of the phase field profile (left) and the pressure profile (right) at different time steps. As seen, the vertical fractures propagate along a straight line until $t = 0.4t_f$. Then, near the inclined natural fractures, the CO₂-driven fractures turns to join them with an angle of approximately 90° at $t = 0.8t_f$. In the last frame 19g, the vertical fractures deviate into the inclined natural fractures and propagate from left tips. This fracture evolving pattern is called ‘crossing with an offset’ which is one possible interaction process of hydraulic fracture and natural fracture [62].

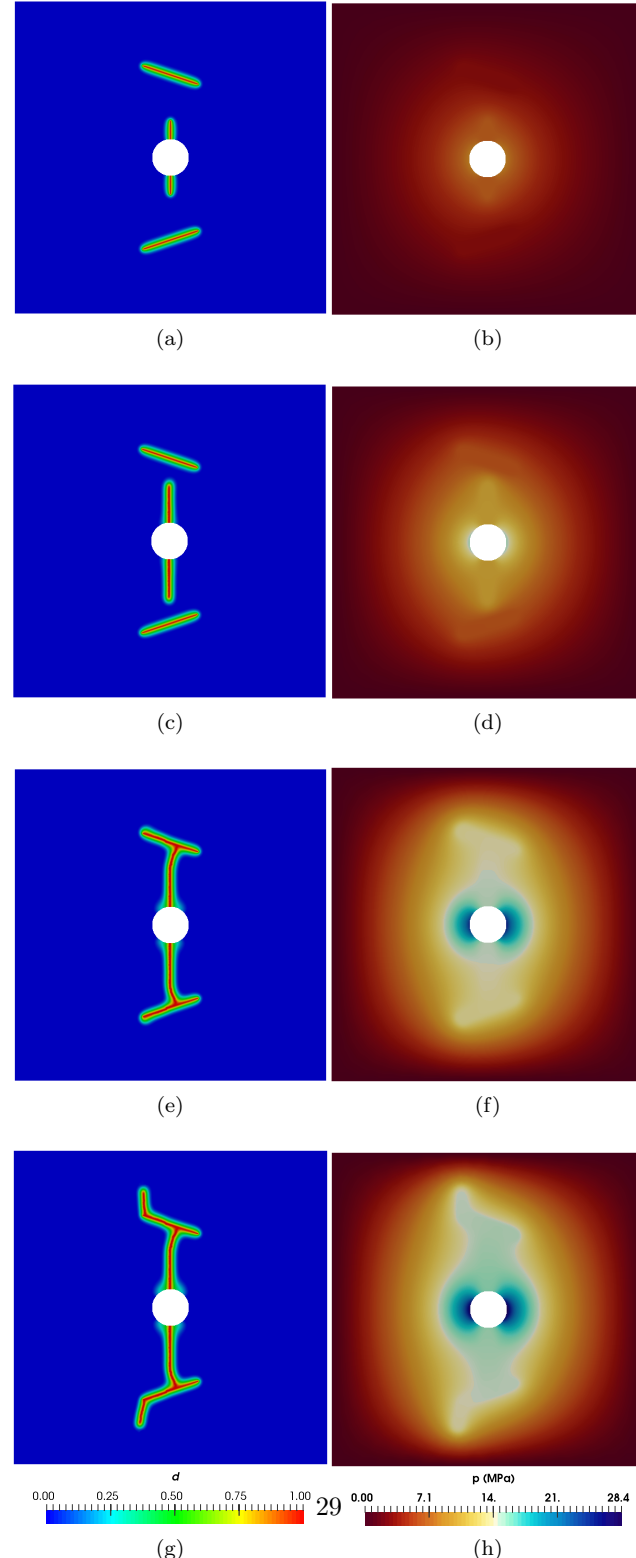


Figure 19: Left: Phase field diagram at different stages (19a) $t = 0.$, (19c) $t = 0.4t_f,$ (19e) $t = 0.8t_f,$ and (19g) $t = t_f.$ Right: Pressure profile at (19b) $t = 0.$, (19d) $t = 0.4t_f,$ (19f) $t = 0.8t_f,$ and (19h) $t = t_f.$ As seen, the vertical fractures propagate along a straight line until they reached the natural fractures. Then, they deviate into the inclined natural fractures, and continue evolving from left tips. ‘Crossing with an offset’ is one possible interaction process of hydraulic fracture and natural fracture [62].

1
2
3
4
5
6
7
8
9 **5. Conclusions**

10 410 We have proposed and verified a phase field approach to simulate CO₂ frac-
11 turing, with CO₂ treated as a compressible fluid. In one of the numerical exam-
12 ples, the breakdown pressure agrees well with widely used analytical solutions.
13 Also, the results agree with experimental results within 30%. While this work
14 represents the first of its kind, potentially the phase field approach allows com-
15 plicated modeling of fracture initiation and branching.
16
17
18
19
20
21
22
23
24
25
26
27
28
29
30
31
32
33
34
35
36
37
38
39
40
41
42
43
44
45
46
47
48
49
50
51
52
53
54
55
56
57
58
59
60
61
62
63
64
65

1
2
3
4
5
6
7
8
9 **Appendix A. Weak forms and discretized formulations**

10 Here we provide weak forms useful for FEniCS implementation. [For more](#)
 11 information on implementing the phase field approach for fracture, see [63].

12 *Appendix A.1. Porous medium*

13 To proceed, let the test function spaces be

$$14 \quad \begin{aligned} \mathcal{V}_u &:= \left\{ \bar{\mathbf{u}} \in H^1(\Omega; \mathbb{R}^2) \mid \bar{\mathbf{u}} = \mathbf{0} \text{ on } \Gamma_D \right\}, \\ 15 \quad \mathcal{V}_d &:= H^1(\Omega). \end{aligned}$$

16 Then we derive the first variations of the energy functional (3), which will be
 17 needed for stating the weak form:

$$18 \quad \delta\Pi_\ell[(\mathbf{u}, d); \bar{\mathbf{u}}] := \int_{\Omega} \boldsymbol{\sigma}[\boldsymbol{\varepsilon}(\mathbf{u}), d] : \boldsymbol{\varepsilon}(\bar{\mathbf{u}}) d\Omega - \int_{\Gamma_N} \mathbf{t}_N \cdot \bar{\mathbf{u}} d\Gamma - \int_{\Omega} \mathbf{b} \cdot \bar{\mathbf{u}} d\Omega \\ 19 \quad + \int_{\Omega} (\alpha - 1) \nabla((1 - d)^2 p) \cdot \bar{\mathbf{u}} d\Omega + \int_{\Omega} (1 - d)^2 \nabla p \cdot \bar{\mathbf{u}} d\Omega \quad (\text{A.1a})$$

$$20 \quad \delta\Pi_\ell[(\mathbf{u}, d); \bar{d}] := \int_{\Omega} (\alpha - 1) g'(d) \bar{d} p \operatorname{div} \mathbf{u} d\Omega + \int_{\Omega} g'(d) \bar{d} \nabla p \cdot \mathbf{u} d\Omega \\ 21 \quad + \int_{\Omega} g'(d) \psi_+(\boldsymbol{\varepsilon}) \bar{d} d\Omega + \frac{g_c}{4c_w} \int_{\Omega} \left(\frac{\omega'(d)}{\ell} \bar{d} + 2\ell \nabla d \cdot \nabla \bar{d} \right) d\Omega. \quad (\text{A.1b})$$

22 The weak form can thus be stated as: Find $(\mathbf{u} \times d) \in \mathcal{S}_{\mathbf{u}} \times \mathcal{S}_d$, such that for all
 23 admissible functions $(\bar{\mathbf{u}} \times \bar{d}) \in \mathcal{V}_{\mathbf{u}} \times \mathcal{V}_d$, $\delta\Pi_\ell[(\mathbf{u}, d); \bar{\mathbf{u}}] = 0$ and $\delta\Pi_\ell[(\mathbf{u}, d); \bar{d}] = 0$.

24 Also we take another variation from (3) which will be needed for the dis-
 25 cretized formulation:

$$26 \quad \delta^2\Pi_\ell[(\mathbf{u}, d); \bar{\mathbf{u}}, \delta\mathbf{u}] = \int_{\Omega} \boldsymbol{\varepsilon}(\delta\mathbf{u}) : \mathbb{C}[\boldsymbol{\varepsilon}(\mathbf{u}), d] : \boldsymbol{\varepsilon}(\bar{\mathbf{u}}) d\Omega, \quad (\text{A.2a})$$

$$27 \quad \delta^2\Pi_\ell[(\mathbf{u}, d); \bar{d}, \delta d] = \int_{\Omega} \delta d g''(d) \psi_+(\boldsymbol{\varepsilon}) \bar{d} d\Omega \\ 28 \quad + \int_{\Omega} (\alpha - 1) g''(d) \bar{d} \delta d p \operatorname{div} \mathbf{u} d\Omega + \int_{\Omega} g''(d) \bar{d} \delta d \nabla p \cdot \mathbf{u} d\Omega \\ 29 \quad + \frac{g_c}{4c_w} \int_{\Omega} \left[\frac{\delta d w''(d) \bar{d}}{\ell} + 2\ell \nabla(\delta d) \cdot \nabla \bar{d} \right] d\Omega, \quad (\text{A.2b})$$

30 where the fourth-order tensor $\mathbb{C}[\boldsymbol{\varepsilon}(\mathbf{u}), d] = \frac{\partial \boldsymbol{\sigma}(\boldsymbol{\varepsilon}, d)}{\partial \boldsymbol{\varepsilon}} \Big|_{\boldsymbol{\varepsilon}=\boldsymbol{\varepsilon}(\mathbf{u})}$ is the tangent elastic-
 31 ity tensor.

32 To discretize the problem, we divide Ω with a conforming mesh \mathcal{T}_h of trian-
 33 gular elements. Let η be the set of nodes of \mathcal{T}_h . We approximate (\mathbf{u}, d) with
 34 the standard P_1 finite element basis functions associated with all nodes $i \in \eta$:

$$35 \quad \mathbf{u}(\mathbf{x}) = \sum_{i \in \eta} \mathbf{N}_i^{\mathbf{u}}(\mathbf{x}) \mathbf{u}_i, \quad d(\mathbf{x}) = \sum_{i \in \eta} N_i(\mathbf{x}) d_i, \quad (\text{A.3})$$

where \mathbf{u}_i , and d_i are the displacement and phase field values at node i , respectively; and $\mathbf{N}_i^{\mathbf{u}}$ is given by:

$$\mathbf{N}_i^{\mathbf{u}} = \begin{bmatrix} N_i & 0 \\ 0 & N_i \end{bmatrix},$$

where N_i is the standard finite element shape function associated with $i \in \eta$, satisfying $N_j(\mathbf{x}_i) = \delta_{ji}$, for all $i, j \in \eta$, and $\mathbf{x}_i, \mathbf{u}_i \in \mathbb{R}^2$ are the position vector and nodal displacement vector of node i , respectively. Note that we also apply the same discretization to the test functions.

Discretized weak form. Let n_{nodes} denote the number of nodes in η . Let $\mathbf{u} \in \mathbb{R}^{2n_{\text{nodes}}}$, $\mathbf{d} \in \mathbb{R}^{n_{\text{nodes}}}$ contain all entries of \mathbf{u}_i , d_i , respectively, for all $i \in \eta$. The discretized residuals can be written as $\mathbb{U}_i(\mathbf{u}) := \delta\Pi(\mathbf{u}; \mathbf{N}_i^{\mathbf{u}}) \in \mathbb{R}^2$ and $\mathbb{D}_i(d) := \delta\Pi(d; N_i) \in \mathbb{R}$ for all $i \in \eta$. With (A.1), these residual vectors are expressed as follows:

$$\begin{aligned} \mathbb{U}_i &= \int_{\Omega} (\mathbf{B}_i)^T \boldsymbol{\sigma}[\boldsymbol{\varepsilon}(\mathbf{u}), d] d\Omega - \int_{\Gamma_N} (\mathbf{N}_i^{\mathbf{u}})^T \mathbf{t}_N d\Gamma - \int_{\Omega} (\mathbf{N}_i^{\mathbf{u}})^T \mathbf{b} d\Omega \\ &\quad + \int_{\Omega} (\alpha - 1)(\mathbf{N}_i^{\mathbf{u}})^T \nabla ((1 - d)^2 p) d\Omega + \int_{\Omega} (\mathbf{N}_i^{\mathbf{u}})^T (1 - d)^2 \nabla p d\Omega \\ \mathbb{D}_i &= \int_{\Omega} (\alpha - 1) g'(d) N_i p \operatorname{div} \mathbf{u} d\Omega + \int_{\Omega} g'(d) N_i (\nabla p)^T \mathbf{u} d\Omega \\ &\quad + \int_{\Omega} g'(d) \psi_+(\boldsymbol{\varepsilon}) N_i d\Omega + \frac{g_c}{4c_w} \int_{\Omega} \left(\frac{w'(d) N_i}{\ell} + 2\ell \nabla d \cdot \nabla N_i \right) d\Omega, \end{aligned} \quad (\text{A.4})$$

where \mathbb{U}_i is also called the nodal force at i . Also note that in (A.4), $\boldsymbol{\sigma}$ is understood as a 3-vector, and the strain-displacement matrix for node i are given by:

$$\mathbf{B}_i = \begin{bmatrix} N_{i,x} & 0 \\ 0 & N_{i,y} \\ N_{i,y} & N_{i,x} \end{bmatrix}.$$

The discretized weak form is $\mathbb{U}_i = \mathbf{0}$ for all nodes i at which \mathbf{u} is not prescribed, and $\mathbb{D}_i = 0$ for all nodes i at which d is not prescribed.

Tangent stiffness matrices. The tangent stiffness matrices are needed for Newton-Raphson algorithms. The tangent stiffness matrix components of (A.2) are $\mathbf{K}_{ij}^u := \partial\mathbb{U}_i/\partial\mathbf{u}_j = \delta^2\Pi[\mathbf{u}; \mathbf{N}_i^{\mathbf{u}}, \mathbf{N}_j^{\mathbf{u}}] \in \mathbb{R}^{2 \times 2}$ for all $i, j \in \eta$ and $K_{ij}^d := \partial\mathbb{D}_i/\partial d_j = \delta^2\Pi[d; N_i, N_j] \in \mathbb{R}$ for all $i, j \in \eta$, which can be expressed as follows:

$$\mathbf{K}_{ij}^u = \int_{\Omega} (\mathbf{B}_i)^T \mathbf{D} \mathbf{B}_j d\Omega, \quad (\text{A.5a})$$

$$\begin{aligned} K_{ij}^d &= \int_{\Omega} (\alpha - 1) g''(d) N_i N_j p \operatorname{div} \mathbf{u} d\Omega + \int_{\Omega} g''(d) N_i N_j (\nabla p)^T \mathbf{u} d\Omega \\ &\quad + \int_{\Omega} g''(d) \psi_+(\boldsymbol{\varepsilon}) N_i N_j d\Omega + \frac{g_c}{4c_w} \int_{\Omega} \left[\frac{w''(d) N_i N_j}{\ell} + 2\ell (\nabla N_i)^T \nabla N_j \right] d\Omega, \end{aligned} \quad (\text{A.5b})$$

where we denote by \mathbf{D} the matrix form of the tangent elastic modulus tensor \mathbb{C} . Below we give its expression $\mathbf{D} = g(d)\mathbf{D}_+ + \mathbf{D}_-$ for our adopted tension-compression decomposition [34]:

$$\mathbf{D}_+ = BH(\text{tr } \boldsymbol{\varepsilon}) \begin{bmatrix} 1 & 1 & 0 \\ 1 & 1 & 0 \\ 0 & 0 & 0 \end{bmatrix} + \frac{G}{3} \begin{bmatrix} 4 & -2 & 0 \\ -2 & 4 & 0 \\ 0 & 0 & 3 \end{bmatrix},$$

$$\mathbf{D}_- = BH(-\text{tr } \boldsymbol{\varepsilon}) \begin{bmatrix} 1 & 1 & 0 \\ 1 & 1 & 0 \\ 0 & 0 & 0 \end{bmatrix},$$

where $B = E/[3(1-2\nu)]$ is the bulk modulus. Here, H is the Heaviside function such that $H(a) = 1$ if $a > 0$, $H(a) = 0$ if $a < 0$, and $H(a) = \frac{1}{2}$ if $a = 0$.

Appendix A.2. Compressible (CO_2) fluid flow discretization

The compressible fluid flow discretization is also done via the finite element method. We first discretize in time and then in space. We will adopt the backward Euler method for time discretization.

To proceed, let the admissible set of pressure be:

$$\mathcal{S}_p := \{p \in H^1(\Omega) | p = p_D \text{ on } \Gamma_P\}.$$

The test function space can be defined as:

$$\mathcal{V}_p := \{\bar{p} \in H^1(\Omega) | \bar{p} = 0 \text{ on } \Gamma_P\}.$$

The weak form can be stated as: find $p \in \mathcal{S}_p$ such that for all admissible functions $\bar{p} \in \mathcal{V}_p$,

$$\begin{aligned} & \frac{1}{\Delta t} \int_{\Omega} \phi(\rho - \rho^{n-1}) \bar{p} \, d\Omega + \frac{1}{\Delta t} \int_{\Omega} \rho(\varepsilon_v - \varepsilon_v^{n-1}) \bar{p} \, d\Omega \\ & + \int_{\Omega} \rho \frac{k(d)}{\mu} \nabla p \cdot \nabla \bar{p} \, d\Omega - \int_{\Gamma_B} Q_g \bar{p} \, d\Gamma = 0, \end{aligned} \quad (\text{A.6})$$

where ρ^{n-1} and ε_v^{n-1} denote solutions at the previous time step.

Also, we use the conventional finite element shape functions $\{N_i\}$ for p :

$$p(\mathbf{x}) = \sum_{i \in \eta} p_i N_i(\mathbf{x}). \quad (\text{A.7})$$

Thus, the residual vector form of A.6 is expressed as follows:

$$\begin{aligned} \mathbb{P}_i := & \frac{1}{\Delta t} \int_{\Omega} \phi(\rho - \rho^{n-1}) N_i \, d\Omega + \frac{1}{\Delta t} \int_{\Omega} \rho(\varepsilon_v - \varepsilon_v^{n-1}) N_i \, d\Omega \\ & + \int_{\Omega} \rho \frac{k(d)}{\mu} (\nabla p)^T \nabla N_i \, d\Omega - \int_{\Gamma_B} Q_g N_i \, d\Gamma. \end{aligned} \quad (\text{A.8})$$

The discretized weak form is $\mathbb{P}_i = 0$ for all nodes i at which p is not prescribed.

The tangent stiffness matrix form of the fluid flow $K_{ij}^p := \partial \mathbb{P}_i / \partial p_j$ for all $i, j \in \eta$, which can be expressed as follows:

$$K_{ij}^p := \int_{\Omega} \rho \frac{k(d)}{\mu} (\nabla N_i)^T \nabla N_j \, d\Omega. \quad (\text{A.9})$$

1
2
3
4
5
6
7
8
9
10
11
12
13
14
15
16
17
18
19
20
21
22
23
24
25
26
27
28
29
30
31
32
33
34
35
36
37
38
39
40
41
42
43
44
45
46
47
48
49
50
51
52
53
54
55
56
57
58
59
60
61
62
63
64
65

Acknowledgments

140 This work is supported by the National Natural Science Foundation of China
with grant #11402146. YS also acknowledges the financial support by the Young
1000 Talent Program of China.

References

- 145 [1] G. Hattori, J. Trevelyan, C. E. Augarde, W. M. Coombs, A. C. Aplin, Numerical simulation of fracking in shale rocks: Current state and future approaches, *Archives of Computational Methods in Engineering* 24 (2) (2017) 281–317.
- 450 [2] R. Middleton, H. Viswanathan, R. Currier, R. Gupta, CO₂ as a fracturing fluid: Potential for commercial-scale shale gas production and CO₂ sequestration, *Energy Procedia* 63 (2014) 7780–7784.
- 455 [3] L. Wang, B. Yao, M. Cha, N. B. Alqahtani, T. W. Patterson, T. J. Kneafsey, J. L. Miskimins, X. Yin, Y.-S. Wu, Waterless fracturing technologies for unconventional reservoirs—opportunities for liquid nitrogen, *Journal of Natural Gas Science and Engineering* 35 (2016) 160–174.
- 460 [4] J. Miller, R. T. Johansen, Fracturing oil shale with explosives for in situ recovery, *Shale Oil, Tar Sands, and Related Fuel Sources* (1976) 98–111.
- 465 [5] A. T. Lillies, S. R. King, Sand fracturing with liquid carbon dioxide, in: SPE Production Technology Symposium, Society of Petroleum Engineers, 1982, pp. SPE-11341-MS.
- 470 [6] Y. Suehiro, M. Nakajima, K. Yamada, M. Uematsu, Critical parameters of $\{x\text{CO}_2 + (1-x)\text{CHF}_3\}$ for $x=(1.0000, 0.7496, 0.5013, \text{ and } 0.2522)$, *The Journal of Chemical Thermodynamics* 28 (10) (1996) 1153–1164.
- 475 [7] D. W. Brown, A hot dry rock geothermal energy concept utilizing supercritical CO₂ instead of water, in: *Proceedings of the twenty-fifth workshop on geothermal reservoir engineering*, Stanford University, 2000, pp. 233–238.
- 480 [8] R. S. Middleton, J. W. Carey, R. P. Currier, J. D. Hyman, Q. Kang, S. Karra, J. Jiménez-Martínez, M. L. Porter, H. S. Viswanathan, Shale gas and non-aqueous fracturing fluids: Opportunities and challenges for supercritical CO₂, *Applied Energy* 147 (2015) 500–509.
- 485 [9] T. Ishida, K. Aoyagi, T. Niwa, Y. Chen, S. Murata, Q. Chen, Y. Nakayama, Acoustic emission monitoring of hydraulic fracturing laboratory experiment with supercritical and liquid CO₂, *Geophysical Research Letters* 39 (16) (2012) L16309.

- 1
2
3
4
5
6
7
8
9 [10] T. Ishida, Y. Chen, Z. Bennour, H. Yamashita, S. Inui, Y. Nagaya, M. Naoi,
10 475 Q. Chen, Y. Nakayama, Y. Nagano, Features of CO₂ fracturing deduced
11 from acoustic emission and microscopy in laboratory experiments, *Journal
12 of Geophysical Research: Solid Earth* 121 (11) (2016) 8080–8098.
13
14 [11] J. Wang, D. Elsworth, Y. Wu, J. Liu, W. Zhu, Y. Liu, The influence of
15 fracturing fluids on fracturing processes: A comparison between water, oil
16 480 and SC-CO₂, *Rock Mechanics and Rock Engineering* 51 (1) (2018) 299–313.
17
18 [12] X. Zhou, T. J. Burbey, Fluid effect on hydraulic fracture propagation be-
19 havior: A comparison between water and supercritical CO₂-like fluid, *Ge-
20 ofluids* 14 (2) (2014) 174–188.
21
22 [13] D. Ngo, A. C. Scordelis, Finite element analysis of reinforced concrete
23 485 beams, *International Concrete Abstracts Portal* 64 (3) (1967) 152–163.
24
25 [14] N. Moës, J. Dolbow, T. Belytschko, A finite element method for crack
26 growth without remeshing, *International Journal for Numerical Methods
27 in Engineering* 46 (1) (1999) 131–150.
28
29 [15] R. Rangarajan, M. M. Chiaramonte, M. J. Hunsweck, Y. Shen, A. J. Lew,
30 490 Simulating curvilinear crack propagation in two dimensions with univer-
31 sal meshes, *International Journal for Numerical Methods in Engineering*
32 102 (3-4) (2015) 632–670.
33
34 [16] C. V. Verhoosel, M. A. Scott, T. J. Hughes, R. De Borst, An isogeometric
35 analysis approach to gradient damage models, *International Journal for
36 Numerical Methods in Engineering* 86 (1) (2011) 115–134.
37
38 [17] B. Bourdin, G. A. Francfort, J.-J. Marigo, Numerical experiments in revis-
39 ited brittle fracture, *Journal of the Mechanics and Physics of Solids* 48 (4)
40 (2000) 797–826.
41
42 [18] R. H. J. Peerlings, R. de Borst, W. A. M. Brekelmans, J. H. P. de Vree,
43 500 Gradient enhanced damage for quasi-brittle materials, *International Jour-
44 nal for Numerical Methods in Engineering* 39 (19) (1996) 3391–3403.
45
46 [19] G. A. Francfort, J.-J. Marigo, Revisiting brittle fracture as an energy min-
47 imization problem, *Journal of the Mechanics and Physics of Solids* 46 (8)
48 (1998) 1319–1342.
49
50 [20] B. Bourdin, C. P. Chukwudzie, K. Yoshioka, A variational approach to
51 the numerical simulation of hydraulic fracturing, in: *SPE Annual Technical
52 Conference and Exhibition*, Society of Petroleum Engineers, 2012, pp. SPE–
53 159154–MS.
54
55 [21] A. Mikelić, M. F. Wheeler, T. Wick, Phase-field modeling of pressurized
56 fractures in a poroelastic medium, *ICES Report* (2014) 14–18.
57
58
59
60
61
62
63
64
65

- [22] K. Yoshioka, B. Bourdin, A variational hydraulic fracturing model coupled to a reservoir simulator, *International Journal of Rock Mechanics and Mining Sciences* 88 (2016) 137–150.
- [23] T. Wick, G. Singh, M. F. Wheeler, Fluid-filled fracture propagation with a phase-field approach and coupling to a reservoir simulator, *SPE Journal* 21 (03) (2016) 981–999.
- [24] S. Mauthe, C. Miehe, Hydraulic fracture in poro-hydro-elastic media, *Mechanics Research Communications* 80 (2017) 69–83.
- [25] W. Ehlers, C. Luo, A phase-field approach embedded in the theory of porous media for the description of dynamic hydraulic fracturing, *Computer Methods in Applied Mechanics and Engineering* 315 (2017) 348–368.
- [26] D. Culp, M. R. Tupek, P. Newell, M. H. Hubler, Phase-field modeling of fracture in CO₂ sequestration, in: 51st US Rock Mechanics/Geomechanics Symposium, American Rock Mechanics Association, 2017, pp. ARMA-2017-0644.
- [27] Y. Heider, B. Markert, Modelling of hydraulic fracturing and fluid flow change in saturated porous domains, *Proc. Appl. Math. Mech.* 17 (1) (2017) 95–98.
- [28] R. Span, W. Wagner, A new equation of state for carbon dioxide covering the fluid region from the triple-point temperature to 1100 K at pressures up to 800 MPa, *Journal of Physical and Chemical Reference Data* 25 (6) (1996) 1509–1596.
- [29] L. Ambrosio, V. M. Tortorelli, On the Approximation of Free Discontinuity Problems, Scuola Normale Superiore, 1990.
- [30] L. Ambrosio, V. M. Tortorelli, On the approximation of functionals depending on jumps by quadratic, elliptic functionals, *Bollettino dell'Unione Matematica Italiana* 6 (1992) 105–123.
- [31] E. Tanné, T. Li, B. Bourdin, J.-J. Marigo, C. Maurini, Crack nucleation in variational phase-field models of brittle fracture, *Journal of the Mechanics and Physics of Solids* 110 (2018) 80–99.
- [32] B. Bourdin, J.-J. Marigo, C. Maurini, P. Sicsic, Morphogenesis and propagation of complex cracks induced by thermal shocks, *Physical Review Letters* 112 (2014) 014301.
- [33] B. Bourdin, C. Chukwudzie, K. Yoshioka, A variational approach to the numerical simulation of hydraulic fracturing, in: M. Jirásek, O. Allix, N. Moës, J. Oliver (Eds.), Computational Modeling of Fracture and Failure of Materials and Structures: Proceedings of CFRAC 2013, 2013, p. 180.

- [34] H. Amor, J.-J. Marigo, C. Maurini, Regularized formulation of the variational brittle fracture with unilateral contact: Numerical experiments, *Journal of the Mechanics and Physics of Solids* 57 (2009) 1209–1229.
- [35] C. Miehe, M. Hofacker, F. Welschinger, A phase field model for rate-independent crack propagation: Robust algorithmic implementation based on operator splits, *Computer Methods in Applied Mechanics and Engineering* 199 (45–48) (2010) 2765–2778.
- [36] F. Javadpour, D. Fisher, M. Unsworth, Nanoscale gas flow in shale gas sediments, *Journal of Canadian Petroleum Technology* 46 (10).
- [37] F. Javadpour, Nanopores and apparent permeability of gas flow in mudrocks (shales and siltstone), *Journal of Canadian Petroleum Technology* 48 (8) (2009) 16–21.
- [38] S. A. Hosseini, F. Javadpour, G. E. Michael, Novel analytical core-sample analysis indicates higher gas content in shale-gas reservoirs, *SPE Journal* 20 (6) (2015) 1–397.
- [39] F. Civan, Effective correlation of apparent gas permeability in tight porous media, *Transport in Porous Media* 82 (2) (2010) 375–384.
- [40] U. Pillai, Y. Heider, B. Markert, A diffusive dynamic brittle fracture model for heterogeneous solids and porous materials with implementation using a user-element subroutine, *Computational Materials Science* 153 (2018) 36 – 47.
- [41] W. Zhu, C. Wei, S. Li, J. Wei, M. Zhang, Numerical modeling on destress blasting in coal seam for enhancing gas drainage, *International Journal of Rock Mechanics and Mining Sciences* 59 (2013) 179 – 190.
- [42] B. Bourdin, G. A. Francfort, J. J. Marigo, The variational approach to fracture, *Journal of Elasticity* 91 (2008) 5–148.
- [43] C. Chukwudozie, Application of the variational fracture model to hydraulic fracturing in poroelastic media, Ph.D. thesis, Louisiana State University (2016).
- [44] A. Mikelić, M. F. Wheeler, Convergence of iterative coupling for coupled flow and geomechanics, *Computational Geosciences* 17 (3) (2013) 455–461.
- [45] A. Logg, G. N. Wells, J. Hake, *DOLFIN: A C++/Python Finite Element Library*, Springer Berlin Heidelberg, Berlin, Heidelberg, 2012.
- [46] P. R. Amestoy, I. S. Duff, J.-Y. L'Excellent, J. Koster, *MUMPS: A general purpose distributed memory sparse solver*, in: *International Workshop on Applied Parallel Computing*, Springer, 2000, pp. 121–130.

1
2
3
4
5
6
7
8
9
10
11
12
13
14
15
16
17
18
19
20
21
22
23
24
25
26
27
28
29
30
31
32
33
34
35
36
37
38
39
40
41
42
43
44
45
46
47
48
49
50
51
52
53
54
55
56
57
58
59
60
61
62
63
64
65

- [47] T. Munson, J. Sarich, S. Wild, S. Benson, L. McInnes, Toolkit for advanced optimization (TAO) users manual, Tech. rep., Technical Report No. ANL/MCS-TM-322-Revision 3.5 (Argonne National Laboratory, 2014) (2014).
- [48] S. Balay, S. Abhyankar, M. F. Adams, J. Brown, P. Brune, K. Buschelman, L. Dalcin, V. Eijkhout, W. D. Gropp, D. Kaushik, M. G. Knepley, D. A. May, L. C. McInnes, R. T. Mills, T. Munson, K. Rupp, P. Sanan, B. F. Smith, S. Zampini, H. Zhang, H. Zhang, PETSc users manual, Tech. Rep. ANL-95/11 - Revision 3.9, Argonne National Laboratory (2018).
- [49] C. Bilgen, A. Kopaničáková, R. Krause, K. Weinberg, A phase-field approach to conchoidal fracture, *Meccanica* 53 (6) (2018) 1203–1219.
- [50] Z. A. Wilson, C. M. Landis, Phase-field modeling of hydraulic fracture, *Journal of the Mechanics and Physics of Solids* 96 (2016) 264–290.
- [51] E. Detournay, D. Garagash, The near-tip region of a fluid-driven fracture propagating in a permeable elastic solid, *Journal of Fluid Mechanics* 494 (2003) 1–32.
- [52] J. Hu, D. Garagash, Plane-strain propagation of a fluid-driven crack in a permeable rock with fracture toughness, *Journal of Engineering Mechanics* 136 (9) (2010) 1152–1166.
- [53] C. Miehe, M. Hofacker, F. Welschinger, A phase field model for rate-independent crack propagation: Robust algorithmic implementation based on operator splits, *Computer Methods in Applied Mechanics and Engineering* 199 (45-48) (2010) 2765–2778.
- [54] M. Ambati, T. Gerasimov, L. De Lorenzis, A review on phase-field models of brittle fracture and a new fast hybrid formulation, *Computational Mechanics* 55 (2) (2015) 383–405.
- [55] C. Miehe, F. Welschinger, M. Hofacker, Thermodynamically consistent phase-field models of fracture: Variational principles and multi-field FE implementations, *International Journal for Numerical Methods in Engineering* 83 (10) (2010) 1273–1311.
- [56] E. Detournay, A.-D. Cheng, Poroelastic response of a borehole in a non-hydrostatic stress field, in: *International Journal of Rock Mechanics and Mining Sciences & Geomechanics Abstracts*, Vol. 25, Elsevier, 1988, pp. 171–182.
- [57] Y. L. Lu, D. Elsworth, L. G. Wang, Microcrack-based coupled damage and flow modeling of fracturing evolution in permeable brittle rocks, *Computers and Geotechnics* 49 (2013) 226–244.
- [58] I. N. Sneddon, M. Lowengrub, *Crack Problems in the Classical Theory of Elasticity*, Wiley, New York, 1969.

1
2
3
4
5
6
7
8
9
10
11
12
13
14
15
16
17
18
19
20
21
22
23
24
25
26
27
28
29
30
31
32
33
34
35
36
37
38
39
40
41
42
43
44
45
46
47
48
49
50
51
52
53
54
55
56
57
58
59
60
61
62
63
64
65

- [59] M. F. Wheeler, T. Wick, W. Wollner, An augmented-Lagrangian method for the phase-field approach for pressurized fractures, *Computer Methods in Applied Mechanics and Engineering* 271 (2014) 69–85.
- [60] M. K. Hubbert, D. G. Willis, *Mechanics of Hydraulic Fracturing*, AAPG Special Volumes, 1972.
- [61] B. Haimson, C. Fairhurst, Initiation and extension of hydraulic fractures in rocks, *Society of Petroleum Engineers Journal* 7 (03) (1967) 310–318.
- [62] C. H. Yew, X. Weng, *Mechanics of Hydraulic Fracturing*, Gulf Professional Publishing, 2014.
- [63] Y. Shen, M. Mollaali, Y. Li, W. Ma, J. Jiang, Implementation details for the phase field approaches to fracture, *Journal of Shanghai Jiaotong University (Science)* 23 (1) (2018) 166–174.